IEEE Access
Multidisciplinary | Rapid Review | Open Access Journal

Received April 17, 2019, accepted April 26, 2019, date of publication April 29, 2019, date of current version May 14, 2019.

Digital Object Identifier 10.1109/ACCESS.2019.2914001

Cloud-Aided Cognitive Ambient Backscatter Wireless Sensor Networks

DONATELLA DARSENA[1], (Senior Member, IEEE), GIACINTO GELLI[2], (Member, IEEE), AND FRANCESCO VERDE[2], (Senior Member, IEEE)

[1]Department of Engineering, Parthenope University, I-80143 Naples, Italy
[2]Department of Electrical Engineering and Information Technology, University of Naples Federico II, I-80125 Naples, Italy

Corresponding author: Francesco Verde (f.verde@unina.it)

This work was supported by the project "Information and Electrical Technologies for e-Health and Industry 4.0" (TecHealth4.0).

ABSTRACT Cognitive ambient backscatter is a wireless communication paradigm that allows a secondary backscatter device to superimpose its information-bearing data on a primary signal, without requiring any type of power-consuming active components or other signal conditioning units. In such a network, the performance of the backscatter system can be severely degraded by channel estimation errors and co-channel direct-link interference (DLI) from the primary system. To overcome these shortcomings, we consider a cloud radio access network (C-RAN) architecture, where both the primary and secondary edge nodes are connected to a cloud processor via high-speed links. In this centralized architecture, secondary edge nodes provide network access to ambient backscatter passive and semi-passive sensors with communication capabilities, and the problem of acquiring channel state information and suppressing the DLI is managed by the cloud processor. In particular, we assess the performance of the secondary backscatter sensor transmission in a realistic system setup, which takes into account training-based channel estimation, practical modulation constraints, and imperfect DLI suppression. In addition, we formulate and solve an optimization problem aimed at maximizing the transmission rate of the secondary transmission, subject to limits on channel estimation error, average symbol error rate, power consumption, and energy storage capabilities of the backscatter sensor. The validity of our analysis and the performance of the secondary system based on the proposed designs are corroborated through the Monte Carlo simulations.

INDEX TERMS Ambient backscatter, cloud radio access network, cognitive radio, data rate maximization, energy harvesting, interference suppression, passive and semi-passive sensors, performance analysis.

I. INTRODUCTION

Driven by the *Internet of Things (IoT)* vision [1], the forthcoming years will be characterized by an explosive growth in the number of sensing devices that need to be connected to the Internet by wireless links. Such massive connectivity requirements must cope with two main limitations: the scarcity of dedicated spectrum portions to allocate sensor transmissions, and the need to reduce, if not eliminate, the communication dependence on batteries.

Since it is commonly recognized that most of the licensed spectrum is underutilized [2], the efficiency of sensor transmissions would greatly benefit from the adoption of *cognitive radio (CR)* approaches. A CR-enabled sensor, being aware of its operational environment, is able to dynamically and autonomously adjust its radio transmission parameters in order to opportunistically perform reliable communications [3], [4]. Furthermore, harvesting energy from external sources might be a solution to improve the lifetime of wireless sensor devices, freeing them from strict battery constraints.

Electrical energy can be harvested [5] by several means, such as: (a) thermal, solar, wind, and vibrational sources; (b) *dedicated* radio-frequency (RF) transmitters (e.g., readers), which are deployed to enable wireless power transfer (WPT) [6]–[14]; (c) *legacy* sources that are not intended for WPT, whose aim is only to ensure wireless information transfer (WIT). The objectives for WPT (i.e., maximization of the energy transmission efficiency) and WIT (i.e., maximization of the information transmission capacity) can be jointly pursued to design sensors with simultaneous wireless information and power transfer (SWIPT) [15], [16].

In recent years, to combine the benefits of CR and SWIPT, new wireless network architectures have been introduced [17], [18], wherein secondary users (SUs) are able

The associate editor coordinating the review of this manuscript and approving it for publication was Abdel-Hamid Soliman.

2169-3536 © 2019 IEEE. Translations and content mining are permitted for academic research only.
Personal use is also permitted, but republication/redistribution requires IEEE permission.
See http://www.ieee.org/publications_standards/publications/rights/index.html for more information.

to harvest energy from primary (i.e., licensed) signals, and use the harvested energy to transmit data to their secondary receivers (SRs). The SUs perform data transmission by temporarily sharing a portion of licensed spectrum, provided that they generate a minimal amount of interference to the primary users (PUs). However, in these CR systems with SWIPT, the SUs employs *active* radios, which are power consuming and, thus, quickly waste the harvested RF energy.

Contrary to active radios, *backscatter devices* [19]–[32] do not need power-consuming and expensive radio analog components (including RF oscillators, amplifiers, and filters), since they modulate information by *reflecting* RF signals. Recently, a novel backscatter technique, referred to as *ambient backscatter communication* (AmBC), has been attracting much attention [19]–[22]. AmBC works by exploiting existing or legacy RF signals (such as TV, radio, cellular, or Wi-Fi systems) for WPT and WIT purposes.

The integration of AmBC into CR networks has been recently considered in [33], [34], by enabling secondary transmitters (STs) to jointly harvest energy from PU signals for basic circuit operations, and perform data transmission by backscattering the PU signals to their SRs. Since signal reflection consumes only a very small power [35], AmBC has the potential to enable moderate-to-high-speed ultra-low-power STs. One of the major problem of integrating AmBC in CR networks stems from the inherent spectrum sharing nature of AmBC: indeed, the performance of the secondary system is adversely affected by direct-link interference (DLI) from the primary transmitter (PT). Moreover, acquisition of channel state information (CSI) in CR networks is a difficult task, due to the lack of cooperation between the primary and secondary systems.

In this paper, to solve these problems, we propose to resort to a *cloud radio access network (C-RAN)* architecture [36], wherein distributed access points, referred to as *edge nodes*, forward user signals to/from a centralized cloud processor (CP) via high-speed wired fronthaul links [37], [38]. The adoption of C-RAN solutions for narrowband IoT (NB-IoT) technology, which support low-power and low-cost devices, has been proven to be feasible in [36], since the relaxed latency requirements and reduced baseband processing complexity allows one to overcome one of the main challenge of C-RAN implementations, namely the capacity requirements of the fronthaul links.

Among other performance gains, the C-RAN solution enables easy CSI acquisition schemes and enhanced interference management capabilities, due to joint baseband processing in the cloud, which, in our scenario, is the key to perform channel estimation and DLI suppression in a simple and effective manner.

A. RELATED WORK

The SU is allowed to operate in dual mode in [33]: in the harvest-then-transmit one, the ST directly sends data towards its SR when the PU is silent, by using the energy harvested during the periods in which the PT is transmitting; in the backscatter one, the ST reflects the PU signal for data transmission when the primary channel is busy. The extension of this scheme to the case of multiple SUs has been developed in [39]. In [33], [39], the STs need active components in the harvest-then-transmit mode, which may be unaffordable for ultra-low-power sensors. Moreover, the optimization framework in [33], [39] is carried out by using information-theoretic performance measures that do not explicitly take into account the DLI from the primary system, as well as channel estimation and practical modulation constraints. To overcome the inherent difficulty in acquiring CSI in AmBC systems, a blind channel estimator has been proposed in [40] relying on the expectation maximization algorithm, whereas clustering-based machine learning algorithms have been employed in [41]. These channel estimation methods are iterative and require appropriate initializations to achieve satisfactory performance.

To eliminate the effect of DLI in AmBC, one possible option consists of shifting the backscattered signal to a frequency band different from that used by the primary system [22]–[24] (so called ''harmonic backscattering''). Besides adding complexity to the ST, this approach requires additional spectrum, which might not be available in many cases. DLI-free transceiver designs have been developed in [31], [42], which exploit the repeating structure of legacy multicarrier signals induced by the use of the cyclic prefix, without increasing the hardware complexity. However, such transceivers require a sufficiently long cyclic prefix so as to ensure a suitably high signal-to-noise ratio (SNR) at the intended recipient of the backscatter data.

Further DLI cancellation methods have been proposed in [34], which exploit the spatial diversity offered by multiple receive antennas at the SR, whereas successive interference cancellation has been advocated in [43]. In [34], complex signal processing techniques are introduced at the SR, however optimization of the harvesting (i.e., power consumption and energy storage capability) and backscatter parameters (i.e., reflection coefficient) of the STs is not considered. On the other hand, time allocation and reflection coefficient optimization for the backscatter system have been derived in [43], by considering a duty cycle with two working states: in the sleep state, the ST does not backscatter any data and stores the energy from the PU signal in a finite-capacity battery for further use; in the active state, the ST backscatters a portion of the PU signal, by simultaneously absorbing the energy of the remaining part to power its circuits. The optimal control policy in [43] has been derived via throughput maximization by tacitly assuming perfect channel estimation and Gaussian-distributed modulations.

B. PROPOSED NETWORK ARCHITECTURE AND MAIN CONTRIBUTIONS

To overcome the problems of channel estimation and DLI suppression in AmBC systems, we propose the network architecture depicted in Fig. 1. The primary edge node (PEN) provides *bidirectional* radio functionalities

(i.e., digital-to-analog conversion, analog-to-digital conversion, power amplification, and filtering) for the signals transmitted/received to/from the PUs within its coverage area. Each PU has its own licensed uplink/downlink channels to communicate with the PEN. We assume that the primary system employs orthogonal frequency-division multiple access (OFDMA) to assign communication resources to the PUs.

The SU is a passive or semi-passive[1] backscatter sensor wishing to transmit data to the cloud by concurrently using the primary channels, which is a scenario of interest for IoT applications [44], [45]. To this end, the sensor backscatters the primary OFDMA signal towards the secondary edge node (SEN), which only provides *unidirectional* radio functionalities from the sensor to the CP, i.e., apart from control signals, it does not transmit data from the cloud to the air.[2]

Baseband signal processing (e.g., coding/decoding, modulation/demodulation, and interference management) is performed by the CP in a centralized manner for both the primary and secondary systems. The capacity requirement for the fronthaul link between the SEN and the CP to transport the baseband signal is low, due to the fact that the backscatter sensor is usually equipped with a single antenna, and, most important, it operates on a low data-rate basis. Moreover, since the backscatter sensor is typically employed in applications with relaxed timing requirements, AmBC performance does not particularly suffer from the latency between the SEN and the CP. On the other hand, since the primary symbols are known at the CP, and the corresponding channel parameters can be estimated through standard techniques, the DLI contribution can be easily subtracted from the received baseband signal. This allows one to drastically alleviate the DLI problem, without resorting to sophisticated multiple-antenna techniques as in [34], which would significantly increase the requirement for fronthaul link capacity in our C-RAN architecture. Additionally, the presence of the ultra-low-power backscatter transmission does not appreciably affect the performance of the primary system [32].

With reference to the architecture of Fig. 1, we study practical designs for the AmBC sensor system operating on frequency-selective block-fading wireless channels. Specifically, contrary to previous papers [33], [39], [43] that assume perfect channel estimation and Gaussian-distributed modulations, we take into account the imperfections due to training-based channel estimation and practical modulation constraints for the secondary AmBC system, as well as imperfect DLI suppression at the CP. In particular, the *average* (with respect to the probability distribution of channel fading) performance of the coherent AmBC detector at the CP is evaluated by means of closed-form formulas. Moreover, unlike [34], we formulate and solve a constrained maximization of the achievable data rate of the sensor transmission with respect to the reflection coefficient, the duty cycle, the cardinality of symbol constellation, and the lengths of the training and data phases of the secondary AmBC sensor, subject to limits on the mean square error of the channel estimate, the average symbol error rate, the power requirements, and the energy storage capabilities.

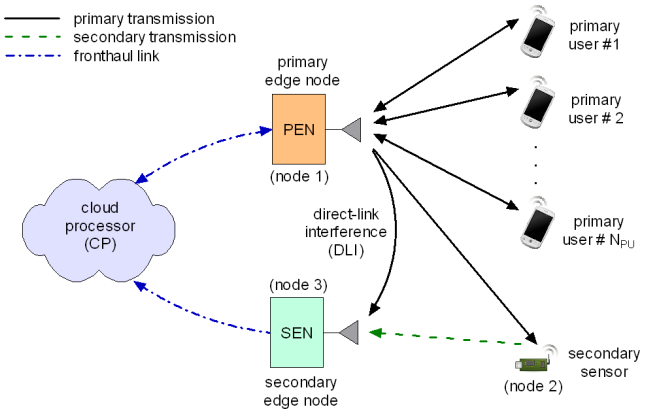

FIGURE 1. The C-RAN architecture integrates CR and AmBC, with N_{PU} primary users and a secondary backscatter sensor. The transmission links from the secondary sensor to the primary users is not explicitly depicted here.

The solution of the constrained maximization is expressed in a simple closed-form (i.e., without the need to resort to iterative algorithms) and involves only *statistical* (rather than instantaneous) network state information, such as the path-loss parameters of the channel and the average energy of the symbol constellation used by the PEN. Finally, numerical Monte Carlo results are also reported, aimed at supporting our theoretical findings and validating the proposed designs.

C. PAPER ORGANIZATION

System and signal models are presented in Section II. The performance analysis of coherent detection of the symbols transmitted by the backscatter system is developed in Section III. Constrained maximization of the achievable data rate of AmBC is carried out in Section IV. Numerical results corroborating our analysis and designs are reported in Section V. Conclusions are drawn in Section VI.

II. SYSTEM MODEL AND BASIC ASSUMPTIONS

In this paper, we refer to the C-RAN architecture depicted in Fig. 1. As in [47], [48], we assume that there exist ideal low-latency fronthaul links with sufficiently large capacity (e.g., optical fiber) connecting the PEN and SEN to the CP, which performs the baseband signal processing and interference management for both the PEN and SEN. As reported in Fig. 1, we focus on the case when the PEN and SEN are spatially-separated devices. However, the proposed framework can be particularized to the case when the PEN and SEN

[1]Sensors can be classified into three categories: active, passive, and semi-passive [16], [35]. Active sensors have internal power sources and they can directly radiate signals, while passive and semi-passive ones can communicate only by reflecting signal transmitted by other devices in the neighborhood.

[2] The case of multiple SUs controlled by the SEN can be recasted in our framework with minor modifications by allowing the SUs to backscatter the OFDMA primary signal in an orthogonal manner, e.g., by accessing the channel on a time-division basis [39], [46].

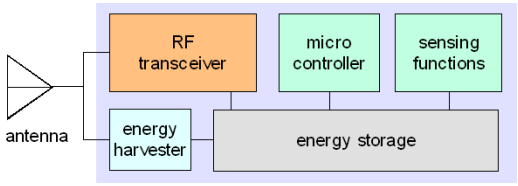

FIGURE 2. A schematic view of a semi-passive sensor. In the case of a passive sensor, there is no energy storage on board.

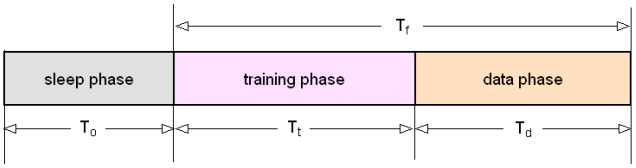

FIGURE 3. Operation scheme of the semi-passive backscatter sensor. In the case of passive backscatter sensor, there is no sleep phase, i.e., $T_o = 0$.

are co-located nodes: in this case, some simplifications occur, e.g., DLI suppression can be directly performed at the edge, thus avoiding to overburden the cloud.

We consider the downlink of an OFDMA primary system, where the PEN, which is equipped with a single antenna, transmits to $N_{\rm PU}$ primary users, each employing a single-antenna transceiver. The primary system employs a total of M subcarriers, divided in $N_{\rm PU}$ disjoint sets such that each subcarrier is assigned to one PU. The primary data block to be transmitted by the PEN within the nth ($n \in \mathbb{Z}$) symbol of length $T_{\rm s}$ is denoted as $\mathbf{s}(n) \triangleq [s^{(0)}(n), s^{(1)}(n), \ldots, s^{(M-1)}(n)]^{\rm T} \in \mathbb{C}^M$, whose entries are modeled as independent and identically distributed (i.i.d.) zero-mean unit-variance phase-shift keying (PSK) symbols; moreover, we assume that $\mathbf{s}(n_1)$ is statistically independent of $\mathbf{s}(n_2)$, for $n_1 \neq n_2$.[3]

The SU is a single-antenna *semi-passive* or *passive* [16] backscatter sensor, which wishes to transmit information-bearing symbols to the cloud by way of the SEN. A semi-passive backscatter sensor is composed of five basic components (Fig. 2):

- the RF front end (including the antenna and the digital multilevel backscatter modulator);
- a module with specific sensing capabilities;
- an energy harvester [49] that converts the RF power into direct current (DC) power;
- a low-power micro-controller;
- an energy storage, e.g., a supercapacitor or a rechargeable battery.

Part of the incoming RF energy from the OFDMA primary transmission is harvested and accumulated into the energy storage of the sensor: such an energy is used to power its sensing and chip operations, while data communication is performed by backscattering the remaining part of the incident radiation. In the case of a passive backscatter sensor, the only difference stems from the fact that the sensor has very little energy storage (typically capacitive) capabilities, which limits the power consumption of the sensor to the average power received by the OFDMA primary transmission that is not backscattered for data communication.

Hereinafter, we assume that time is slotted in *periods*: the harvesting and backscatter processes are carried out by the sensor on a period-by-period basis. With reference to a semi-passive backscatter sensor, we assume that, at the beginning of each period, the energy storage is empty and, therefore, the sensor is in *sleep mode* until it harvests a sufficient amount of energy to power its chip reliably; when the harvested energy is larger than a given threshold, the sensor switches to the *wake mode* in order to perform sensing tasks and data communication. More precisely, as illustrated in Fig. 3, each period is divided into three slots:

- *Sleep phase* ($T_{\rm o}$ s): the sensor only harvests energy while consuming negligible chip power. Such an energy is accumulated in the storage: if the average harvested RF energy is sufficient, the sensor wakes up and the following two phases occur; otherwise, it remains in sleep mode.
- *Training phase* ($T_{\rm t}$ s): the sensor sends training symbols to the cloud for channel estimation, by reflecting a part of the OFDMA primary signal back to the SEN, whereas the remaining energy is absorbed by the harvester.
- *Data phase* ($T_{\rm d}$ s): it is similar to the training phase, but the sensor transmits information-bearing symbols.

The length of the training and data phases is $T_{\rm f} = T_{\rm t} + T_{\rm d}$, referred to as the *frame duration*, whereas $T_{\rm p} = T_{\rm o} + T_{\rm f}$ is the *period duration*. The *duty cycle* of the backscatter sensor is thus defined as

$$D \triangleq \frac{T_{\rm f}}{T_{\rm p}} = \left(1 + \frac{T_{\rm o}}{T_{\rm f}}\right)^{-1}. \tag{1}$$

When the backscatter sensor is passive, due to the absence of an energy storage, in each period there are only training and data phases of duration $T_{\rm t}$ and $T_{\rm d}$, respectively. In this case, the modulator and the sensing module are powered only by the portion of the OFDMA signal power that is not backscattered during such phases, i.e., $T_{\rm o} = 0$, which implies that $T_{\rm p} = T_{\rm f}$ and $D = 1$. In the subsequent signal models, we refer to the case when the backscatter sensor is semi-passive; the corresponding equations for a passive sensor can be obtained as a special case by setting $T_{\rm o} = 0$.

A. SIGNAL MODEL

According to Fig. 1, we will refer to the PEN, the backscatter secondary sensor, and the SEN as nodes 1, 2, and 3, respectively. The primary symbol vector $\mathbf{s}(n)$ is subject to conventional OFDMA precoding, encompassing M-point inverse discrete Fourier transform (IDFT), followed by cyclic prefix insertion of length $L < M$. The data block transmitted by the

[3]The assumption that the PEN transmits PSK symbols is made only to streamline the subsequent performance analysis. The proposed framework can be straightforwardly extended to other linear modulation formats.

PEN can be expressed [50] as

$$\mathbf{u}(n) \triangleq [u^{(0)}(n), u^{(1)}(n), \ldots, u^{(P-1)}(n)]^{\mathrm{T}} = \mathbf{T}_{\mathrm{cp}}\, \mathbf{W}_{\mathrm{IDFT}}\, \mathbf{s}(n) \tag{2}$$

where $P \triangleq M + L$ and $\mathbf{T}_{\mathrm{cp}} \triangleq [\mathbf{I}_{\mathrm{cp}}^{\mathrm{T}}, \mathbf{I}_M]^{\mathrm{T}} \in \mathbb{R}^{P\times M}$, with $\mathbf{I}_{\mathrm{cp}} \in \mathbb{R}^{L\times M}$ obtained from $\mathbf{I}_M$ by picking its last L rows, and $\mathbf{W}_{\mathrm{IDFT}} \in \mathbb{C}^{M\times M}$ is the unitary symmetric IDFT matrix [50]. The correlation matrix $\mathbb{E}[\mathbf{u}(n)\,\mathbf{u}^{\mathrm{H}}(n)]$ of the vector $\mathbf{u}(n)$ is given by $\mathbf{T}_{\mathrm{cp}}\,\mathbf{T}_{\mathrm{cp}}^{\mathrm{T}}$, which is asymptotically equivalent to $\mathbf{I}_P$ in weak norm [51], for sufficiently large values of M. We will rely on such an equivalence by assuming that, in the large M limit, the entries of $\mathbf{u}(n)$ are i.i.d. zero-mean unit-variance circularly symmetric complex random variables. The data vector $\mathbf{u}(n)$ undergoes parallel-to-serial (P/S) conversion, and the resulting sequence $u(n)$, which is defined by $u(n\,P+p) = u^{(p)}(n)$, for $p \in \mathcal{P} \triangleq \{0, 1, \ldots, P-1\}$, feeds a digital-to-analog converter (DAC), operating at sampling rate $1/T_{\mathrm{c}} \triangleq P/T_{\mathrm{s}}$, where T_{c} is the sampling period.

We consider channel models that take into account both small- and large-scale fading. The generic $i \to k$ communication link in Fig. 1 is modeled as a linear time-varying random system with complex baseband impulse response $\widetilde{c}_{ik}(t,\tau)$ (including also the impulse response of the DAC and receiving filters). We assume that, for a fixed τ, the channel impulse response (CIR) $\widetilde{c}_{ik}(t,\tau)$ is approximately constant within frame intervals of length T_{f}. Hence, we can consider the CIR $\widetilde{c}_{ik}^{(h)}(\tau) \triangleq \widetilde{c}_{ik}(hT_{\mathrm{f}},\tau)$ in the discrete-time variable $h \in \mathbb{Z}$. A block fading channel model is assumed, which implies that $\widetilde{c}_{ik}^{(h)}(\tau)$ for a fixed τ is a sequence of independent random variables with respect to h. On the other hand, for a given h, the CIR $\widetilde{c}_{ik}^{(h)}(\tau)$ is modeled as a zero-mean circularly symmetric complex Gaussian random process [52], with autocorrelation function

$$\mathbb{E}[\widetilde{c}_{ik}^{(h)}(\tau)\widetilde{c}_{ik}^{(h)}(\tau')^*] = \sigma_{ik}^2\, \widetilde{p}_{ik}(\tau)\, \delta(\tau-\tau') \tag{3}$$

where σ_{ik}^2 is the reciprocal of the average path-loss of the $i \to k$ link, $\delta(\tau-\tau')$ captures the statistical independence among path delays (so called *uncorrelated scattering* [52]), with $\delta(t)$ being the Dirac delta function, $\widetilde{p}_{ik}(\tau)$ is the power delay profile (PDP), which is normalized so as to have unitary area; in the following, we assume a uniform [4] PDP for $\tau \in [0, L_{ik}\,T_{\mathrm{c}}]$, with $L_{ik} \in \{0, 1, \ldots, L\}$, where $L_{ik}\,T_{\mathrm{c}}$ is the maximum multipath spread of the channel [52].

The $i \to k$ link is also characterized by a time offset (TO) $\Delta_{ik} = \theta_{ik}\,T_{\mathrm{c}} + \zeta_{ik} \ll T_s$, with $\theta_{ik} \in \mathbb{N}$ and $\zeta_{ik} \in [0, T_{\mathrm{c}})$. It is assumed that L_{ik} and θ_{ik} obey $L_{ik} + \theta_{ik} \leq P-1$, which ensures that the nth received block over the $i \to k$ link is impaired only by the *interblock* interference of the previous one. Finally, all the discrete-time channels are assumed to be statistically independent of the primary and secondary symbols, and CIRs of different links are statistically independent among themselves, i.e., $\widetilde{c}_{i_1k_1}^{(h)}(\tau)$ and $\widetilde{c}_{i_2k_2}^{(h)}(\tau)$ are statistically independent, for $i_1 \neq i_2$ or $k_1 \neq k_2$.

[4] The framework at hand can be easily generalized to the case of a non-uniform PDP.

1) SIGNAL TRANSMITTED BY THE BACKSCATTER SENSOR

The baseband continuous-time OFDMA primary signal received by the backscatter sensor is given by

$$\widetilde{r}_2(t) = \sqrt{2\,\mathcal{P}_{\mathrm{s}}} \sum_{\ell=-\infty}^{+\infty} u(\ell)\, \widetilde{c}_{12}^{(h)}(t - \Delta_{12} - \ell\,T_{\mathrm{c}}) \tag{4}$$

for $t \in [h\,T_{\mathrm{f}}, (h+1)\,T_{\mathrm{f}})$, where $\mathcal{P}_{\mathrm{s}}$ is the average transmission RF power (including the gain of the transmit antenna),[5] the noise at the sensor has been neglected, since its integrated circuit only consists of passive components and involves simple signal processing operations [35], [53].

In both the semi-passive and passive cases, the digital multilevel backscatter modulator [54], [55] allows one to vary the chip impedance of the backscatter sensor, thus causing changes in the reflection coefficient. Let the chip impedance of the sensor assume Q distinct values Z_q^{c}, for $q \in \{1, 2, \ldots, Q\}$, the *power wave reflection coefficient* Γ_q corresponding to the qth chip impedance is given by

$$\Gamma_q = \frac{(Z^{\mathrm{a}})^* - Z_q^{\mathrm{c}}}{Z^{\mathrm{a}} + Z_q^{\mathrm{c}}} \tag{5}$$

where Z^{a} denotes the antenna impedance.[6] During the training and data phases, the signaling interval of the backscatter sensor is equal to T_s, i.e., it transmits in backscatter mode only one symbol for each OFDMA symbol of the primary system.

The symbols $b(n)$ are modeled as a sequence of i.i.d. zero-mean unit-variance circularly symmetric random variables, drawn from a Q_{t}-order constellation $\{\beta_{\mathrm{t},1}, \beta_{\mathrm{t},2}, \ldots, \beta_{\mathrm{t},Q_{\mathrm{t}}}\}$ during the training phase or from a Q_{d}-order constellation $\{\beta_{\mathrm{d},1}, \beta_{\mathrm{d},2}, \ldots, \beta_{\mathrm{d},Q_{\mathrm{d}}}\}$ during the data phase. Training and data symbols modulate the backscattered signal by changing the chip impedances. Indeed, by virtue of (5), the qth chip impedance Z_q^{c} corresponds to the point β_q of the symbol constellation by means of the one-to-one mapping

$$\Gamma_q = \alpha\,\beta_q \tag{6}$$

where $0 < \alpha \leq 1$ is a constant related to the power wave reflection coefficient, and $\beta_q \equiv \beta_{\mathrm{t},q}$ and $Q \equiv Q_{\mathrm{t}}$ during the training phase, whereas $\beta_q \equiv \beta_{\mathrm{d},q}$ and $Q \equiv Q_{\mathrm{d}}$ during the data phase. In the sequel, we set $T_{\mathrm{t}} = B_{\mathrm{t}}\,T_{\mathrm{s}}$ and $T_{\mathrm{d}} = B_{\mathrm{d}}\,T_{\mathrm{s}}$, with $B_{\mathrm{t}}, B_{\mathrm{d}} \in \mathbb{N}$.

The complex envelope of the continuous-time backscattered signal can be modeled [32], [54], [55] as follows

$$\widetilde{x}_2(t) = \widetilde{r}_2(t)\,\Gamma(t), \quad \text{for } t \in [T_{\mathrm{o}}, T_{\mathrm{o}} + T_{\mathrm{f}}) \tag{7}$$

with

$$\Gamma(t) = \alpha \sum\nolimits_{q=0}^{B_{\mathrm{t}}+B_{\mathrm{d}}-1} b(q)\, \widetilde{\psi}_2(t - T_{\mathrm{o}} - q\,T_{\mathrm{s}}) \tag{8}$$

where $\widetilde{\psi}_2(t)$ is a rectangular unit-amplitude symbol-shaping function, i.e., $\widetilde{\psi}_2(t) = 1$ for $0 \leq t \leq T_{\mathrm{s}}$ and zero otherwise.

[5] $\mathcal{P}_{\mathrm{s}}$ is the so-called effective isotropic radiated power (EIRP) of the PEN.

[6] When the backscatter sensor is semi-passive, the chip impedance is matched to the antenna impedance during the sleep phase. In this circumstance, all the input energy is harvested and there is no backscattered field.

Since the backscatter process is implemented with passive components [54], the sequence $b(n)$ is subject to the amplitude constraint $|b(n)| \leq 1, \forall n \in \mathbb{Z}$.

2) SIGNAL RECEIVED BY THE SEN

Since the backscatter sensor simply remodulates the carrier of the PEN in backscatter mode, it is reasonable to assume that the carrier frequency offset over the $2 \rightarrow 3$ link is negligible. Moreover, we will refer hereinafter to the frame $[T_o, T_o + T_f)$, without loss of generality. Thus, we will drop the time index h in the CIR $\widetilde{c}_{ik}^{(h)}(\tau)$ and model the $i \rightarrow k$ link by the random process $\widetilde{c}_{ik}(\tau)$ in the delay variable τ. Under the above assumptions, the baseband version of the continuous-time signal picked up by the SEN reads as

$$\widetilde{r}_3(t) = \widetilde{x}_2(t) * \widetilde{c}_{23}(t - \Delta_{23}) + \widetilde{\imath}_3(t) + \widetilde{v}_3(t) \tag{9}$$

for $t \in [T_o, T_o + T_f)$, where $*$ denotes (linear) convolution, $\widetilde{\imath}_3(t) = \sqrt{2\,\mathcal{P}_s} \sum_{\ell=-\infty}^{+\infty} u(\ell)\widetilde{c}_{13}(t - \Delta_{13} - \ell\, T_c)$ is the DLI contribution, and $\widetilde{v}_3(t)$ represents thermal noise.[7]

We assume that the multipath spread of the $1 \rightarrow 2$ and $2 \rightarrow 3$ links is much smaller than the symbol period T_s of the backscatter transmission, i.e., $L_{12}, L_{23} \ll P$. In this case, taking into account (4), (7), (8), and (9), one can write

$$\begin{aligned}\widetilde{x}_2(t) * \widetilde{c}_{23}(t-\Delta_{23}) &= [\widetilde{r}_2(t)\,\Gamma(t)] * \widetilde{c}_{23}(t-\Delta_{23}) \\ &\approx \Gamma(t-\Delta_{23})\,[\widetilde{r}_2(t) * \widetilde{c}_{23}(t-\Delta_{23})] \\ &= \sqrt{2\,\mathcal{P}_s}\,\Gamma(t-\Delta_{23}) \\ &\quad \times \sum_{\ell=-\infty}^{+\infty} u(\ell)\,\widetilde{c}_{123}(t-\Delta_{12}-\Delta_{23}-\ell\, T_c)\end{aligned} \tag{10}$$

for $t \in [T_o, T_o + T_f)$, where $\widetilde{c}_{123}(\tau) \triangleq \widetilde{c}_{12}(\tau) * \widetilde{c}_{23}(\tau) \equiv 0$ for $\tau \notin [0, (L_{12} + L_{23})\, T_c)$. The SEN performs sampling of the received signal (9) and cyclic prefix removal in order not to increase the requirement for fronthaul link capacity.

The signal (9) is sampled with rate $1/T_c$, at time epochs $t_{n,p} \triangleq T_o + n\, T_s + p\, T_c$, with $p \in \mathcal{P}$. Taking into account (10), it can be shown [32] that, if the SEN discards the first L samples of (9) and collects the remaining ones in $\widetilde{\mathbf{r}}_3(n) \triangleq [\widetilde{r}_3(t_{n,L}), \widetilde{r}_3(t_{n,L+1}), \ldots, \widetilde{r}_3(t_{n,P-1})]^T \in \mathbb{C}^M$, one has the vector model

$$\widetilde{\mathbf{r}}_3(n) = \alpha\, \widetilde{\mathbf{h}}(n)\, b(n) + \widetilde{\boldsymbol{\imath}}_3(n) + \widetilde{\mathbf{v}}_3(n) \tag{11}$$

for $n \in \{0, 1, \ldots, B_t + B_d - 1\}$, provided that

$$\begin{aligned} L_{12}+L_{23}+\theta_{12}+\theta_{23} &\leq P-1 \\ L &\geq \max(L_{13}+\theta_{13}+1, L_{23}+\theta_{23}+1, \\ &\quad L_{12}+L_{23}+\theta_{12}+\theta_{23}+1) \end{aligned} \tag{12}$$

with

$$\widetilde{\mathbf{h}}(n) \triangleq \sqrt{2\,\mathcal{P}_s}\, \mathbf{R}_{cp}\, \widetilde{\mathbf{C}}_{12}^{(0)}\, \widetilde{\mathbf{C}}_{23}^{(0)}\, \mathbf{u}(n) \in \mathbb{C}^M \tag{13}$$

[7]Following a common practice (see, e.g., [57]), it is assumed in the sequel that the structural-dependent term of the scattered field [58] has been removed at the SEN before transmitting the baseband data to the CP.

$$\widetilde{\boldsymbol{\imath}}_3(n) \triangleq \sqrt{2\,\mathcal{P}_s}\, \mathbf{R}_{cp}\, \widetilde{\mathbf{C}}_{13}^{(0)}\, \mathbf{u}(n) \in \mathbb{C}^M \tag{14}$$

where $\mathbf{R}_{cp} \triangleq [\mathbf{O}_{M\times L}, \mathbf{I}_M] \in \mathbb{R}^{M\times P}$ and

$$\widetilde{\mathbf{C}}_{ik}^{(0)} \triangleq \sum_{\ell=0}^{L_{ik}} c_{ik}(\ell)\, \mathbf{F}^{\ell+\theta_{ik}} \in \mathbb{C}^{P\times P} \tag{15}$$

is the Toeplitz lower-triangular [59] channel matrix corresponding to the samples $c_{ik}(\ell) \triangleq \widetilde{c}_{ik}(\ell\, T_c + \zeta_{ik})$ of the $i \rightarrow k$ link, with $\mathbf{F}$ denoting the Toeplitz *forward shift* matrix [59], and $\widetilde{\mathbf{v}}_3(n) \triangleq [\widetilde{v}_3(t_{n,L}), \widetilde{v}_3(t_{n,L+1}), \ldots, \widetilde{v}_3(t_{n,P-1})]^T \in \mathbb{C}^M$. It is noteworthy that, according to (3), the order of the causal finite-impulse response $c_{ik}(\ell)$ is L_{ik}, i.e., $c_{ik}(\ell) \equiv 0$ for $\ell \notin \{0, 1, \ldots, L_{ik}\}$. Moreover, in the sequel, we assume that $\mathbb{E}[\widetilde{\mathbf{v}}_3(n_1)\widetilde{\mathbf{v}}_3^H(n_2)] = \mathbf{O}_{P\times P}$, for $n_1 \neq n_2 \in \mathbb{Z}$.

The vector $\widetilde{\mathbf{r}}_3(n)$ is transmitted from the SEN to the CP over a low-latency high-capacity fronthaul link. After performing the DFT at the CP, one gets

$$\mathbf{r}_3(n) \triangleq \mathbf{W}_{DFT}\, \widetilde{\mathbf{r}}_3(n) = \alpha\, \mathbf{h}(n)\, b(n) + \boldsymbol{\imath}_3(n) + \mathbf{v}_3(n) \tag{16}$$

for $n \in \{0, 1, \ldots, B_t+B_d-1\}$, where $\mathbf{W}_{DFT} \triangleq \mathbf{W}_{IDFT}^{-1}$ defines the unitary symmetric DFT matrix [50], the vectors

$$\mathbf{h}(n) \triangleq \mathbf{W}_{DFT}\, \widetilde{\mathbf{h}}(n) = \sqrt{2\,\mathcal{P}_s}\, \mathbf{C}_{12}\, \mathbf{C}_{23}\, \mathbf{s}(n) \in \mathbb{C}^M \tag{17}$$

$$\boldsymbol{\imath}_3(n) \triangleq \sqrt{2\,\mathcal{P}_s}\, \mathbf{C}_{13}\, \mathbf{s}(n) \in \mathbb{C}^M \tag{18}$$

are the backscatter channel and DLI contribution seen by the CP, respectively, the nonzero entries of the diagonal matrix $\mathbf{C}_{ik} \triangleq \mathrm{diag}[C_{ik}(0), C_{ik}(1), \ldots, C_{ik}(M-1)]$ are defined as

$$C_{ik}(m) \triangleq e^{-j\frac{2\pi}{M}\theta_{ik}m} \sum_{\ell=0}^{L_{ik}} c_{ik}(\ell)\, e^{-j\frac{2\pi}{M}\ell m} \tag{19}$$

for $m \in \mathcal{M} \triangleq \{0, 1, \ldots, M-1\}$, and $\mathbf{v}_3(n) \triangleq \mathbf{W}_{DFT}\, \widetilde{\mathbf{v}}_3(n)$.

III. PERFORMANCE ANALYSIS OF AMBC

The task of the CP is to *coherently* estimate the data symbols $b(B_t), b(B_t + 1), \ldots, b(B_t + B_d - 1)$, relying on the observation of the sampled received signal (16) for $n \in \{0, 1, \ldots, B_t + B_d - 1\}$ and on knowledge of the training symbols $b(0), b(1), \ldots, b(B_t - 1)$. Compared to conventional active transmissions, performance analysis of such a coherent estimation process for AmBC in fading channels is complicated by the non-Gaussian nature of the composite backscatter channel (17) and by the presence of the DLI term (18). In the forthcoming subsections, we develop a performance analysis of the channel estimator and the data detector, by explicitly taking into account the DLI cancellation process at the CP.

A. DLI CANCELLATION

In the proposed centralized C-RAN architecture, the CP has perfect knowledge of the RF power $\mathcal{P}_s$ and of the symbol vector $\mathbf{s}(n)$. In this case, the parameters related to $\widetilde{c}_{13}(t)$ and Δ_{13} of the $1 \rightarrow 3$ link can be jointly estimated [56] when the sensor does not backscatter [20], [21] and, hence, the DLI contribution $\boldsymbol{\imath}_3(n)$ can be subtracted from (16) in the cloud.

Let $\overline{n} \notin \{0, 1, \ldots, B_{\rm t}+B_{\rm d}-1\}$ be the index of a given symbol period wherein the backscatter sensor is silent, i.e., $\alpha = 0$, eq. (16) ends up to

$$\mathbf{r}_3(\overline{n}) = \sqrt{2\,\mathcal{P}_{\rm s}}\,\mathbf{C}_{13}\,\mathbf{s}(\overline{n}) + \mathbf{v}_3(\overline{n}) \tag{20}$$

and the following identity holds

$$\sqrt{2\,\mathcal{P}_{\rm s}}\,\mathbf{C}_{13}\,\mathbf{s}(\overline{n}) = \mathbf{S}(\overline{n})\,\mathbf{W}_{\rm DFT}\,\mathbf{P}\,\boldsymbol{\gamma}_{13} = \boldsymbol{\Upsilon}(\overline{n})\,\boldsymbol{\gamma}_{13} \tag{21}$$

where $\mathbf{S}(\overline{n}) \triangleq \sqrt{2\,\mathcal{P}_{\rm s}\,M}\,\mathrm{diag}[s^{(0)}(\overline{n}), s^{(1)}(\overline{n}), \ldots, s^{(M-1)}(\overline{n})]$ is a *known* nonsingular diagonal matrix, the full-column rank matrix $\mathbf{P} \triangleq [\mathbf{I}_L, \mathbf{O}^{\rm T}_{(M-L)\times L}]^{\rm T} \in \mathbb{R}^{M\times L}$ is also known, the vector $\boldsymbol{\gamma}_{13} \triangleq \mathbf{D}_{13}\,\mathbf{c}_{13} \in \mathbb{C}^L$ collects all the unknown parameters, with

$$\mathbf{D}_{13} \triangleq [\mathbf{O}^{\rm T}_{\theta_{13}\times(L_{13}+1)}, \mathbf{I}_{L_{13}+1}, \mathbf{O}^{\rm T}_{(L-\theta_{13}-L_{13}-1)\times(L_{13}+1)}]^{\rm T} \tag{22}$$

$$\mathbf{c}_{13} \triangleq [c_{13}(0), c_{13}(1), \ldots, c_{13}(L_{13})]^{\rm T} \in \mathbb{C}^{L_{13}+1}. \tag{23}$$

Moreover, we have set $\boldsymbol{\Upsilon}(\overline{n}) \triangleq \mathbf{S}(\overline{n})\,\mathbf{W}_{\rm DFT}\,\mathbf{P} \in \mathbb{C}^{M\times L}$ in (21).

Under the assumption that $\mathbf{v}_3(n) \sim \mathcal{CN}(\mathbf{0}_M, \sigma^2_{v_3}\,\mathbf{I}_M)$, for each $n \in \mathbb{Z}$, the *maximum likelihood (ML) estimation* of $\boldsymbol{\gamma}_{13}$ is given [60] by[8]

$$\widehat{\boldsymbol{\gamma}}_{13} = \boldsymbol{\Upsilon}^{\dagger}(\overline{n})\,\mathbf{r}_3(\overline{n}) = \boldsymbol{\gamma}_{13} + \boldsymbol{\Upsilon}^{\dagger}(\overline{n})\,\mathbf{v}_3(\overline{n}) \tag{24}$$

where the superscript † denotes the Moore-Penrose generalized inverse and we have used the fact that $\boldsymbol{\Upsilon}^{\dagger}(\overline{n})\,\boldsymbol{\Upsilon}(\overline{n}) = \mathbf{I}_L$. As a matter of fact, the estimator (24) does not require exact knowledge of the channel order L_{13}.

After estimating $\boldsymbol{\gamma}_{13}$ according to (24), the DLI contribution in (16) can be subtracted at the CP as follows

$$\mathbf{z}_3(n) \triangleq \mathbf{r}_3(n) - \boldsymbol{\Upsilon}(n)\,\widehat{\boldsymbol{\gamma}}_{13} = \alpha\,\mathbf{h}(n)\,b(n) + \mathbf{d}_3(n) \tag{25}$$

for $n \in \{0, 1, \ldots, B_{\rm t}+B_{\rm d}-1\}$, where the *disturbance* vector

$$\mathbf{d}_3(n) \triangleq \mathbf{v}_3(n) - \boldsymbol{\Upsilon}(n)\,\boldsymbol{\Upsilon}^{\dagger}(\overline{n})\,\mathbf{v}_3(\overline{n}) \tag{26}$$

accounts for both noise and imperfect DLI cancellation. It is seen that $\mathbf{d}_3(n)$ is a zero-mean random vector with $\mathbb{E}[\mathbf{d}_3(n_1)\,\mathbf{d}^{\rm H}_3(n_2)] = \mathbf{O}_{M\times M}$, for $n_1 \neq n_2 \in \mathbb{Z}$, whereas

$$\mathbf{R}_{\mathbf{d}_3\mathbf{d}_3} \triangleq \mathbb{E}[\mathbf{d}_3(n)\,\mathbf{d}^{\rm H}_3(n)] = \sigma^2_{v_3}\left(1 + \frac{L}{M}\right)\mathbf{I}_M. \tag{27}$$

B. CHANNEL ESTIMATION

Coherent detection of the symbols transmitted by the backscatter sensor during the data phase requires knowledge of the composite channel vector $\mathbf{h}(n)$ in (25). Since the symbol blocks $\mathbf{s}(n)$, for $n \in \{0, 1, \ldots, B_{\rm t}+B_{\rm d}-1\}$, are known at the CP, such a problem boils down to estimate the diagonal entries of $\mathbf{C}_{12}\,\mathbf{C}_{23}$, which is performed by using the training symbols transmitted by the backscatter sensor.

Let $\mathbf{z}_{\rm t} \triangleq [\mathbf{z}_3(0), \mathbf{z}_3(1), \ldots, \mathbf{z}_3(B_{\rm t}-1)]^{\rm T} \in \mathbb{C}^{B_{\rm t}M}$ collect the samples received by the CP in the training phase, one has

$$\mathbf{z}_{\rm t} = \mathbf{T}\,\mathbf{W}_{\rm DFT}\,\mathbf{P}\,\mathbf{D}_{123}\,\mathbf{c}_{123} + \mathbf{d}_{\rm t} \tag{28}$$

[8]The estimator (24) is unbiased and attains the Cramer-Rao lower bound. Hence, it represents the minimum variance unbiased estimator [60].

where $\mathbf{T} \triangleq \sqrt{M}\,[\mathbf{T}^{\rm T}(0), \mathbf{T}^{\rm T}(1), \ldots, \mathbf{T}^{\rm T}(B_{\rm t}-1)]^{\rm T}$, with $\mathbf{T}(n)$ being the *known* nonsingular diagonal matrix associated with the vector $\alpha\,\sqrt{2\,\mathcal{P}_{\rm s}}\,\mathbf{s}(n)\,b(n)$, the matrix

$$\mathbf{D}_{123} \triangleq [\mathbf{O}^{\rm T}_{(\theta_{12}+\theta_{23})\times(L_{12}+L_{23}+1)}, \mathbf{I}_{L_{12}+L_{23}+1}, \mathbf{O}^{\rm T}_{(L-\theta_{12}-\theta_{23}-L_{12}-L_{23}-1)\times(L_{12}+L_{23}+1)}]^{\rm T} \tag{29}$$

is full-column rank, the vector $\mathbf{c}_{123} \in \mathbb{C}^{L_{12}+L_{23}+1}$ collects the samples of the convolution between $\{c_{12}(\ell)\}_{\ell=0}^{L_{12}}$ and $\{c_{23}(\ell)\}_{\ell=0}^{L_{23}}$, and $\mathbf{d}_{\rm t} \triangleq [\mathbf{d}_3(0), \mathbf{d}_3(1), \ldots, \mathbf{d}_3(B_{\rm t}-1)]^{\rm T} \in \mathbb{C}^{B_{\rm t}M}$ collects all the disturbance contributions. Henceforth, channel acquisition boils down to estimating from (28) the vector $\boldsymbol{\gamma}_{123} \triangleq \mathbf{D}_{123}\,\mathbf{c}_{123} \in \mathbb{C}^L$, which collects all the unknowns.

An estimate $\widehat{\boldsymbol{\gamma}}_{123}$ of $\boldsymbol{\gamma}_{123}$ can be obtained from (28) by resorting to the *least squares (LS) estimator* [60], which is given by

$$\widehat{\boldsymbol{\gamma}}_{123} = (\mathbf{T}\,\mathbf{W}_{\rm DFT}\,\mathbf{P})^{\dagger}\mathbf{z}_{\rm t} = \boldsymbol{\gamma}_{123} + (\mathbf{T}\,\mathbf{W}_{\rm DFT}\,\mathbf{P})^{\dagger}\mathbf{d}_{\rm t} \tag{30}$$

where we have observed that $(\mathbf{T}\,\mathbf{W}_{\rm DFT}\,\mathbf{P})^{\dagger}(\mathbf{T}\,\mathbf{W}_{\rm DFT}\,\mathbf{P}) = \mathbf{I}_L$. It is noteworthy that, in principle, the LS estimator (30) exists even if only a single training symbol is sent by the sensor, i.e., $B_{\rm t} = 1$, and it does not require exact knowledge of the orders of the $1 \to 2$ and $2 \to 3$ links.

After estimating $\boldsymbol{\gamma}_{123}$ through (30), the corresponding estimate $\widehat{\mathbf{h}}(n)$ of $\mathbf{h}(n)$ can be computed as

$$\widehat{\mathbf{h}}(n) = \sqrt{2\,\mathcal{P}_{\rm s}}\,\mathrm{diag}\left(\sqrt{M}\,\mathbf{W}_{\rm DFT}\,\mathbf{P}\,\widehat{\boldsymbol{\gamma}}_{123}\right)\mathbf{s}(n). \tag{31}$$

A performance measure of the LS estimator (30) is the *mean square error (MSE)* $\Delta_{\rm mse} \triangleq \mathbb{E}[\|\widehat{\boldsymbol{\gamma}}_{123} - \boldsymbol{\gamma}_{123}\|^2]$, which can be evaluated as reported in the following Theorem.

Theorem 1: The MSE of estimator (30) is given by

$$\Delta_{\rm mse} = \sigma^2_{d_3}\left[\frac{2\,\alpha^2\,\mathcal{P}_{\rm s}\,M}{L}\sum_{n=0}^{B_{\rm t}-1}|b(n)|^2\right]^{-1} \tag{32}$$

where

$$\sigma^2_{d_3} \triangleq \sigma^2_{v_3}\left(1 + \frac{L}{M}\right). \tag{33}$$

Proof: See Appendix A. ■

Eq. (32) shows that $\Delta_{\rm mse}$ is a decreasing function of the number $B_{\rm t}$ of training symbols transmitted by the backscatter sensor. In the particular case when $b(n)$ is drawn from a PSK constellation, i.e., $|b(n)|^2 = 1$, for any $n \in \{0, 1, \ldots, B_{\rm t}-1\}$, it follows from (32) that

$$\Delta_{\rm mse} = \frac{\sigma^2_{d_3}\,L}{2\,\alpha^2\,\mathcal{P}_{\rm s}\,M\,B_{\rm t}} \tag{34}$$

which depends on known system parameters and on the constant α, which is related to the power wave reflection coefficient of the backscatter sensor.

C. DATA DETECTION

The coherent detector at the CP must estimate the data symbols transmitted by the backscatter sensor by using the channel estimate (31). Obviously, the channel estimation error contributes to degrade the detection performance. In principle, one can first evaluate the symbol error probability (SEP) at the output of the detector, given $\mathbf{h}(n)$ and $\widehat{\mathbf{h}}(n)$, and, then, average the obtained result with respect to the joint probability distribution of $\mathbf{h}(n)$ and $\widehat{\mathbf{h}}(n)$. However, such an approach does not lead to a closed-form expression even for Gaussian-distributed channels [61].

Since we are interested in obtaining manageable closed-form performance results, useful for design purposes, we follow a more pragmatic approach: specifically, we evaluate the average SEP (ASEP) $\overline{P}(e)$ by assuming that $\widehat{\mathbf{h}}(n) = \mathbf{h}(n)$, by choosing the backscatter parameters α and B_t so as to ensure a negligible channel estimation error (see Section IV). The validity of such an approach will be shown in Section V.

Let $\widetilde{\mathbf{c}}_{ik} \triangleq [C_{ik}(0), C_{ik}(1), \ldots, C_{ik}(M-1)]^\mathrm{T} \in \mathbb{C}^M$, for any $i, k \in \{1, 2\}$ with $i \neq k$, and set

$$\mathbf{s}_\mathrm{t} \triangleq [\mathbf{s}^\mathrm{T}(B_\mathrm{t}), \mathbf{s}^\mathrm{T}(B_\mathrm{t}+1), \ldots, \mathbf{s}^\mathrm{T}(B_\mathrm{t}+B_\mathrm{d}-1)]^\mathrm{T}. \tag{35}$$

For $n \in \{B_\mathrm{t}, B_\mathrm{t}+1, \ldots, B_\mathrm{t}+B_\mathrm{d}-1\}$, according to (25), it can be verified that $\mathbf{d}_3(n) \sim \mathcal{CN}[\mathbf{0}_M, \sigma_{v_3}^2\, \mathbf{K}_{\mathbf{d}_3\mathbf{d}_3}(n)]$, conditioned on $\mathbf{s}(\overline{n})$ and $\mathbf{s}_\mathrm{t}$, where

$$\mathbf{K}_{\mathbf{d}_3\mathbf{d}_3}(n) \triangleq \mathbf{I}_M + \frac{1}{2\,\mathcal{P}_\mathrm{s}\,M}\boldsymbol{\Upsilon}(n)\,\boldsymbol{\Upsilon}^\mathrm{H}(n) \tag{36}$$

is a positive definite matrix. On the other hand, given $\mathbf{s}(\overline{n})$ and $\mathbf{s}_\mathrm{t}$, the disturbance vectors $\mathbf{d}_3(n_1)$ and $\mathbf{d}_3(n_2)$ are statistically correlated, i.e.,

$$\mathbb{E}\left[\mathbf{d}_3(n_1)\,\mathbf{d}_3^\mathrm{H}(n_2)\,\middle|\,\mathbf{s}(\overline{n}), \mathbf{s}_\mathrm{t}\right] = \frac{\sigma_{v_3}^2}{2\,\mathcal{P}_\mathrm{s}\,M}\boldsymbol{\Upsilon}(n_1)\,\boldsymbol{\Upsilon}^\mathrm{H}(n_2). \tag{37}$$

for $n_1 \neq n_2$. In the sequel, we will neglect such a correlation, which is a reasonable assumption when $2\,\mathcal{P}_\mathrm{s}\,M \gg \sigma_{v_3}^2$, and consider one-shot detection, by using the following statistic for detecting the symbols transmitted by the sensor:

$$\begin{aligned}\rho_3(n) &\triangleq \mathbf{h}^\mathrm{H}(n)\,\mathbf{K}_{\mathbf{d}_3\mathbf{d}_3}^{-1}(n)\,\mathbf{z}_3(n)\\ &= \alpha\,\mathbf{h}^\mathrm{H}(n)\,\mathbf{K}_{\mathbf{d}_3\mathbf{d}_3}^{-1}(n)\,\mathbf{h}(n)\,b(n) + \mathbf{h}^\mathrm{H}(n)\,\mathbf{K}_{\mathbf{d}_3\mathbf{d}_3}^{-1}(n)\,\mathbf{d}_3(n)\end{aligned} \tag{38}$$

for $n \in \{B_\mathrm{t}, B_\mathrm{t}+1, \ldots, B_\mathrm{t}+B_\mathrm{d}-1\}$. Moreover, we assume that the symbols transmitted by the backscatter sensor during the data phase are drawn from a square quadrature amplitude modulation (QAM) constellation.

Let $P(e; n)$ denote the symbol error probability (SEP) at the output of the ML detector of the CP in the nth symbol period, given $\mathbf{s}(n)$, $\mathbf{s}(\overline{n})$, $\widetilde{\mathbf{c}}_{12}$, and $\widetilde{\mathbf{c}}_{23}$, and define $A_1 \triangleq 4\left[1-(1/\sqrt{Q_\mathrm{d}})\right]$ and $A_2 \triangleq 6\,\gamma_\mathrm{d}/(Q_\mathrm{d}-1)$, with $\log_2(Q_\mathrm{d})$ being an even number, where $\gamma_\mathrm{d} \triangleq 1/\sigma_{v_3}^2$ is the average SNR per data symbol. Conditioned on $\mathbf{s}(n)$, $\mathbf{s}(\overline{n})$, $\widetilde{\mathbf{c}}_{12}$, and $\widetilde{\mathbf{c}}_{23}$, it results that $\mathbf{h}^\mathrm{H}(n)\,\mathbf{K}_{\mathbf{d}_3\mathbf{d}_3}^{-1}(n)\,\mathbf{d}_3(n) \sim \mathcal{CN}[0, \sigma_{v_3}^2\,\mathbf{h}^\mathrm{H}(n)\,\mathbf{K}_{\mathbf{d}_3\mathbf{d}_3}^{-1}(n)\,\mathbf{h}(n)]$. Hence, according to the nearest neighbor bound [52], which is a tight approximation to the SEP in the high-SNR regime, one gets

$$P(e; n) \approx \frac{A_1}{2}\,\mathrm{erfc}\left(\sqrt{\frac{A_2}{2}\,\alpha^2\,\mathbf{h}^\mathrm{H}(n)\,\mathbf{K}_{\mathbf{d}_3\mathbf{d}_3}^{-1}(n)\,\mathbf{h}(n)}\right) \tag{39}$$

where $\mathrm{erfc}(x)$ is the complementary error function. Approximation (39) can be regarded as an upper bound on the SEP of the ML detector for a non-square QAM constellation [52].

As a performance measure of the detection process, we provide in Theorem 2 an upper bound on the ASEP, which is the expected value $\overline{P}(e)$ of $P(e; n)$ in (39) over the sample space of $\{\mathbf{s}(n), \widetilde{\mathbf{c}}_{12}, \widetilde{\mathbf{c}}_{23}\}$. Under our assumptions, the samples $c_{ik}(0), c_{ik}(1), \ldots, c_{ik}(L_{ik})$ are modeled as independent zero-mean circularly symmetric complex Gaussian random variables, with $\mathbb{E}[|c_{ik}(\ell)|^2] = \sigma_{ik}^2/(L_{ik}+1)$.

Theorem 2: It results that $\overline{P}(e) \leq \overline{P}_\mathrm{upper}(e)$, with

$$\overline{P}_\mathrm{upper}(e) \triangleq A_1\left[f\left(\frac{A_2}{2}\,\alpha^2\,\mathcal{P}_\mathrm{s}\,\sigma_{12}^2\,\sigma_{23}^2\right)\right]^M \tag{40}$$

where

$$f(A) \triangleq -\frac{1}{A}\,\exp\left(\frac{1}{A}\right)\,\mathrm{Ei}\left(-\frac{1}{A}\right) \tag{41}$$

with, for $x < 0$,

$$\mathrm{Ei}(x) \triangleq \int_{-\infty}^{x}\frac{\exp(u)}{u}\,\mathrm{d}u = \chi + \ln(-x) + \sum_{k=1}^{+\infty}\frac{x^k}{k!\,k} \tag{42}$$

$$\chi \triangleq \lim_{n\to\infty}\left(n^{-1}\sum_{k=1}^{n}k^{-1} - \ln n\right) \approx 0.57721 \tag{43}$$

being the exponential integral function and the Euler-Mascheroni constant, respectively.

Proof: See Appendix B. ■

It is interesting to observe that, since $f(A) \approx \ln(A)/A$ for $A \gg 1$, the ASEP $\overline{P}(e)$ tends to zero with the same order of $[\ln(\mathcal{P}_\mathrm{s})/\mathcal{P}_\mathrm{s}]^M$ as the transmit power of the primary system grows without bound, i.e., $\mathcal{P}_\mathrm{s} \to +\infty$. This shows that the performance of the AmBC system exhibits a diversity order equal to the number M of subcarriers of the primary system.

IV. MAXIMIZATION OF THE AMBC DATA RATE

In this section, we deal with the problem of maximizing the number of bits transmitted by the backscatter sensor per frame, i.e., the *data rate* of the secondary transmission, which is defined as

$$R_\mathrm{b} \triangleq \frac{B_\mathrm{d}\,\log_2(Q_\mathrm{d})}{T_\mathrm{f}} \tag{44}$$

where $T_\mathrm{f} = T_\mathrm{t} + T_\mathrm{d}$ is assumed to be fixed and depends on the coherence time of the fading channels. The data rate is a function of the following variables:

- the constant α related to the power wave reflection coefficient of the backscatter sensor through (6);

- the cardinality $Q_{\rm d}$ of the information-bearing backscatter symbol constellation;[9]
- the length of the training and data phases, i.e., $T_{\rm t}$ and $T_{\rm d}$ and, additionally, the duty cycle (i.e., $T_{\rm o}$) only when the backscatter sensor is semi-passive.[10]

Since a backscatter sensor is not typically able to perform sophisticated channel estimation and/or to process large amount of feedback information sent by the SEN, we focus on constrained maximization problems of $R_{\rm b}$ that involve, in addition to the noise figure of the SEN/CP, only *statistical* knowledge at the backscatter sensors, such as the variances of the $1 \to 2$ and $2 \to 3$ links and the average energy of the symbol constellation used by the PEN.

In this respect, we capitalize on the performance analysis results in Section III: specifically, we impose that $\Delta_{\rm mse}$ in (32) and $\overline{P}_{\rm upper}(e)$ in (40) are below given target values $\Delta_{\rm target}$ and $\overline{P}_{\rm target}(e)$, respectively, i.e., $\overline{P}(e) \leq \overline{P}_{\rm upper}(e) \leq \overline{P}_{\rm target}(e)$ and $\Delta_{\rm mse} \leq \Delta_{\rm target}$. Moreover, we assume that the cardinality of the QAM constellation of the backscatter modulator is upper bounded by $Q_{\max} \triangleq 2^{q_{\max}}$, with $q_{\max} \in \mathbb{N}$. Finally, we account for the energy storage and circuit energy consumption constraints at the backscatter sensor, as explained in the following subsection. Then, we formulate and solve the proposed constrained data rate maximization problem, which encompasses both passive and semi-passive sensors.

A. ENERGY HARVESTING, CONSUMPTION AND STORAGE

According to the law of energy conservation (see, e.g., [62]), the average RF energy $\mathcal{E}_{\rm o}$ harvested by a semi-passive backscatter sensor during the sleep phase is proportional to that of the received signal (4), i.e.,[11]

$$\mathcal{E}_{\rm o} = \eta\, \mathcal{P}_{\rm rx}\, T_{\rm o} \tag{45}$$

which is accumulated in the energy storage, where $0 < \eta \leq 1$ denotes the *harvesting efficiency*,

$$\mathcal{P}_{\rm rx} \triangleq \frac{1}{2}\, \langle \mathbb{E}\left[|\widetilde{r}_2(t)|^2 \right] \rangle = \sigma_{12}^2\, G_{\rm rx}\, \mathcal{P}_{\rm s} \tag{46}$$

is the average RF power of the received signal (4), $G_{\rm rx}$ is the antenna gain of the sensor, and $\langle \cdot \rangle$ denotes infinite-time temporal averaging. In the sequel, we set $T_{\rm o} = B_{\rm o}\, T_{\rm s}$ (see Fig. 3), which may exceed the coherence time of the channel.

In the training and data phases, a part of energy of the received OFDMA primary signal is still harvested, while the remaining received signal is backscattered to the receiver. The average RF energy $\mathcal{E}_{\rm h}$ harvested by the backscatter sensor during the transmission of the generic symbol $b(n)$, for $n \in \{0, 1, \ldots, B_{\rm t} + B_{\rm d} - 1\}$, reads as $\mathcal{E}_{\rm h} = \mathcal{P}_{\rm h}\, T_{\rm s}$, which does not depend on the symbol index n, where $\mathcal{P}_{\rm h} \triangleq \eta\,(1-\alpha^2)\,\mathcal{P}_{\rm rx}$ is the average harvested RF power. Therefore, the total average harvested energy $\mathcal{E}_{\rm tot}$ during the sleep, training, and data phases amounts to

$$\mathcal{E}_{\rm tot} = \mathcal{E}_{\rm o} + (B_{\rm t} + B_{\rm d})\, \mathcal{E}_{\rm h} = \eta\, \mathcal{P}_{\rm rx} \left[T_{\rm o} + (1 - \nu\alpha^2)\, T_{\rm f} \right]. \tag{47}$$

In practice, there is a *minimum* voltage needed to reliably power the backscatter sensor. Typically, for a semi-passive sensor, the circuit energy consumption in the sleep phase can be neglected. Let $\mathcal{P}_{\rm tot}$ be the total DC power consumption of the backscatter sensor during the training and data phases, we impose that, in the case of a semi-passive sensor, the total harvested energy in the sleep, training, and data phases is not smaller than the circuit energy consumption, i.e., $\mathcal{E}_{\rm tot} \geq \mathcal{P}_{\rm tot}\, T_{\rm f}$, thus leading to the following constraint on α:

$$\alpha^2 \leq \alpha_{\max}^2 + \frac{T_{\rm o}}{T_{\rm f}} \tag{48}$$

where

$$\alpha_{\max}^2 \triangleq 1 - \frac{\mathcal{P}_{\rm tot}}{\eta\, \mathcal{P}_{\rm rx}} \tag{49}$$

is a fixed threshold that limits the amount of the incident RF signal that is backscattered to the SEN. In the sequel, we assume that the primary transmit power $\mathcal{P}_{\rm s}$ and the variance of the $1 \to 2$ link are such that $\alpha_{\max}^2 > 0$, otherwise the backscatter sensor cannot work at all. When the backscatter sensor is passive, there is no energy storage on board and, in this case, the circuit energy consumption constraint can be obtained from (48) by setting $T_{\rm o} = 0$.

When the backscatter sensor is a semi-passive sensor, it is equipped (see Fig. 2) with an energy storage of maximum capacity $\mathcal{E}_{\max}$. Since the excess energy cannot be conserved in the energy storage anyway, we impose the energy storage constraint $\mathcal{E}_{\rm tot} \leq \mathcal{E}_{\max}$ for a semi-passive backscatter sensor, thus yielding the following additional constraint on α:

$$\alpha^2 \geq \alpha_{\rm storage}^2 + \frac{T_{\rm o}}{T_{\rm f}} \tag{50}$$

with

$$\alpha_{\rm storage}^2 \triangleq 1 - \frac{\mathcal{E}_{\max}}{\eta\, \mathcal{P}_{\rm rx}\, T_{\rm f}}. \tag{51}$$

We underline that no energy storage constraint has to be imposed for a passive backscatter sensor, i.e., $\mathcal{E}_{\max} = 0$.

B. DATA RATE OPTIMIZATION

At this point, we are in the position to optimize the relevant backscatter parameters α, $Q_{\rm d}$, $T_{\rm o}$, $T_{\rm t}$, and $T_{\rm d}$ so as to maximize the data rate (44). For a semi-passive backscatter sensor, we formulate the following constrained optimization problem:

$$(\alpha^\star, Q_{\rm d}^\star, T_{\rm o}^\star, T_{\rm t}^\star, T_{\rm d}^\star) = \arg \max_{\alpha, Q_{\rm d}, T_{\rm o}, T_{\rm t}, T_{\rm d}} R_{\rm b}\, T_{\rm s} \ \text{ s.t.}$$

[9] The cardinality $Q_{\rm t}$ of the training symbols is assumed to be fixed. Indeed, training symbols are typically chosen from lower-order constellations in order to simplify their optimal design and achieve robust channel estimation.

[10] We remember that the duty cycle is equal to one (i.e., $T_{\rm o} = 0$) in the case of a passive backscatter sensor.

[11] In general, the output power of the harvester is a nonlinear function of its input power [63]. Herein, the amount of harvested energy at the sensor is assumed to be linearly proportional to the received signal power. This is a widely-used simplification in the literature that can be seen as an approximation of the nonlinear model when the input power is greater than the harvester's sensitivity threshold and smaller than its saturation power.

$$\begin{aligned} D &\geq D_{\min}, \quad \text{with } D \text{ defined in (1)}, \\ \alpha^2 &\leq \alpha^2_{\max} + \frac{T_o}{T_f}, \quad \text{with } \alpha_{\max} \text{ defined in (49)}, \\ \alpha^2 &\geq \alpha^2_{\text{storage}} + \frac{T_o}{T_f}, \quad \text{with } \alpha^2_{\text{storage}} \text{ defined in (51)}, \\ \Delta_{\text{mse}} &\leq \Delta_{\text{target}}, \quad \text{with } \Delta_{\text{mse}} \text{ given in (32)}, \\ \overline{P}_{\text{upper}}(e) &\leq \overline{P}_{\text{target}}(e), \quad \text{with } \overline{P}_{\text{upper}}(e) \text{ given in (40)}, \\ T_t + T_d &= T_f, \quad 0 < \alpha \leq 1, \quad Q_d \leq Q_{\max}, \\ T_o &> 0, \quad T_t > 0, \quad \text{and} \quad T_d > 0 \end{aligned} \tag{52}$$

where the normalization of R_b by $1/T_s$ has been introduced for mathematical convenience. It should be noted that the constraint $D \geq D_{\min}$, with $0 < D_{\min} \leq 1$, is imposed to prevent T_o from increasing without bound, thus avoiding that the backscatter sensor remains in sleep mode for a long time and transmits few data with high transmit power.

Assuming that the training symbols sent by the backscatter sensor are PSK one, the optimization problem (52) admits the closed-form solution reported in Theorem 3.

Theorem 3: For PSK training symbols, the solution of (52) is given by

$$\alpha^\star = \min\left[\sqrt{\alpha^2_{\max} + I_{\max}}, \sqrt{\Gamma_d\,(Q_{\max} - 1)}, 1\right] \tag{53}$$

$$Q_d^\star = \min\left[1 + \frac{(\alpha^\star)^2}{\Gamma_d}, Q_{\max}\right] \tag{54}$$

$$T_o^\star = [(\alpha^*)^2 - \alpha^2_{\max}]\,T_f \tag{55}$$

$$T_t^\star = \frac{\Gamma_t}{(\alpha^\star)^2}, \quad T_d^\star = T_f - T_t^\star \tag{56}$$

where $\Gamma_d \triangleq \left\{\sigma^2_{v_3} f^{-1}\left([\overline{P}_{\text{target}}(e)/4]^{1/M}\right)\right\}/(3\,\mathcal{P}_s\,\sigma^2_{12}\,\sigma^2_{23})$, $\Gamma_t \triangleq (\sigma^2_{d_3}\,L\,T_s)/(M\,\mathcal{P}_s\,\Delta_{\text{target}})$, $I_{\max} \triangleq (1 - D_{\min})/D_{\min}$, with $\alpha^2_{\max} \geq \alpha^2_{\text{storage}}$ and $\Gamma_t/T_f \leq \alpha^2_{\max} + I_{\max}$.[12]

Proof: See Appendix C. ■

If $Q_d^\star$ given by (54) turns out to be smaller than 2, there is no solution for the given requirements. For a passive backscatter sensor, the optimal values of the parameters $\alpha^\star$, $Q_d^\star$, $T_t^\star$, and $T_d^\star$ can be obtained by Theorem 3 by setting $T_o^\star = 0$, $D_{\min} = 1$, and discarding the condition $\alpha^2_{\max} \geq \alpha^2_{\text{storage}}$.

It is noteworthy that the optimal parameters (53)-(56) can be calculated *off-line* – since their evaluation does not require instantaneous network state information – and they remain fixed as long as the relevant system specifications do not change significantly. In particular, it is interesting to observe that the optimal value of α in (53), which greatly influences the values of all the remaining parameters, can assume three possible values: (i) according to (1) and (48), when $(\alpha^\star)^2 = \alpha^2_{\max} + I_{\max}$, the sensor harvests the minimum amount of energy to feed its circuit, i.e., $\mathcal{E}_{\text{tot}} = \mathcal{P}_{\text{tot}}\,T_f$; (ii) when $(\alpha^\star)^2 = \Gamma_d\,(Q_{\max} - 1)$, the sensor sends back just that part of the impinging primary signal that allows to transmit data by using the largest cardinality of the QAM constellation, while ensuring $\overline{P}_{\text{upper}}(e) = \overline{P}_{\text{target}}(e)$; (iii) according to (6), when $\alpha^\star = 1$, the sensor reflects the entire incident field back to the SEN, resulting thus in maximum backscatter signal strength. Once $\alpha^\star$ has been calculated, for each point β_q of the backscatter symbol constellation, the corresponding value of Γ_q can be obtained from (6), with $q \in \{1, 2, \ldots, Q\}$, and, consequently, the chip impedance of the sensor can be designed by solving (5) with respect to Z_q^c.

[12] According to (49) and (51), inequality $\alpha^2_{\max} \geq \alpha^2_{\text{storage}}$ is equivalent to $\mathcal{E}_{\max} \geq \mathcal{P}_{\text{tot}}\,T_f$, which is a very mild condition in many cases.

V. MONTE CARLO PERFORMANCE ANALYSIS

In all the Monte Carlo simulations, the following common setting is considered. The primary system is an OFDMA system with $M = 128$ subcarriers and cyclic prefix length $L = 16$, thus implying $P = M + L = 144$, which employs quaternary PSK (QPSK) modulation and operates at $f_{\text{carrier}} = 2.4$ GHz, with sampling period $T_c = 25$ ns and symbol period $T_s = 3.6\,\mu$s. Unless otherwise specified, the primary EIRP is $\mathcal{P}_s = 33$ dBm. According to III-C, we simulated a Rayleigh fading scenario and we adopted the following path-loss model (see e.g. [64])):

$$\sigma^2_{ik} = \sigma^2_{\text{ref}}\left(\frac{1}{d_{ik}}\right)^\kappa \tag{57}$$

where $\sigma^2_{\text{ref}} = \lambda^2_{\text{carrier}}/(4\pi)^2$, with λ_{carrier} denoting the carrier wavelength, $\kappa = 1.6$ is the path-loss exponent (typical of an indoor scenario) and d_{ik} is the distance between nodes i and k, with $i \neq k$. The order of the discrete-time channels is set equal to $L_{12} = L_{23} = 4$, whereas the corresponding time offsets are fixed to $\theta_{12} = \theta_{23} = 0$, respectively. The noise variance $\sigma^2_{v_3}$ is -100 dBm.

The backscatter sensor employs a QPSK modulation for training (i.e., $Q_t = 4$) and a Q_d-QAM modulation for data, wherein all symbols are equiprobably chosen. The transmission parameters α, Q_d, T_o, T_t, and T_d of the sensor are the result of the optimization procedure discussed in Section IV. The frame length T_f is equal to $B_f = 100$ symbol periods. In the semi-passive case, the backscatter sensor is assumed to be equipped with a tiny battery of 100 mAh for 1.25 V [65], to which it corresponds a maximum capacity of $\mathcal{E}_{\max} = 450$ J. Unless otherwise specified, the total DC power consumption of the sensor in wake mode is $\mathcal{P}_{\text{tot}} = -36$ dBm [66] and, with reference to the semi-passive case, the duty-cycle threshold is $D_{\min} = 0.8$. The energy conversion efficiency is assumed to be $\eta = 0.6$. The ASEP and channel MSE targets are assumed to be equal to $\overline{P}_{1,\text{target}}(e) = \Delta_{\text{target}} = 10^{-4}$, and we set $Q_{\max} = 256$.

As performance measures for the backscatter system, we evaluated both the data rate R_b defined in eq. (44) and the error probability (ASEP). Data detection is based on the ML rule described in Subsection III-C, which employs the estimate (31) of the channel vector $\mathbf{h}(n)$ obtained by training. The ASEP has been obtained by carrying out 10^5 independent trials, with each run using a different set of symbols, channel parameters, and noise samples.

In Figs. 4–9, we report the coverage map of the proposed AmBC system, i.e., the values of the data rate R_b that can be achieved by a passive sensor located at coordinates (x, y),

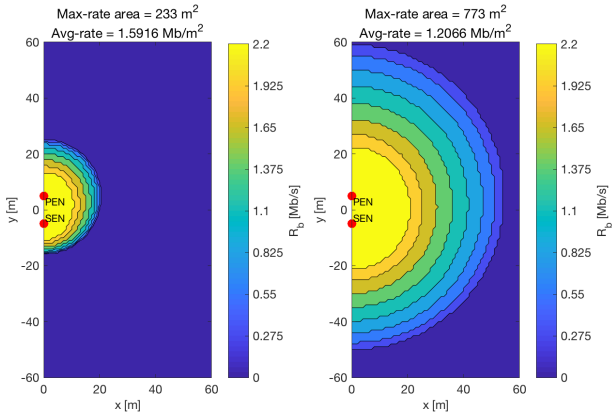

FIGURE 4. AmBC coverage map (passive case; PEN-SEN distance = 10 m) for EIRP = 26 dBm (left-side plot) and EIRP = 33 dBm (right-side plot).

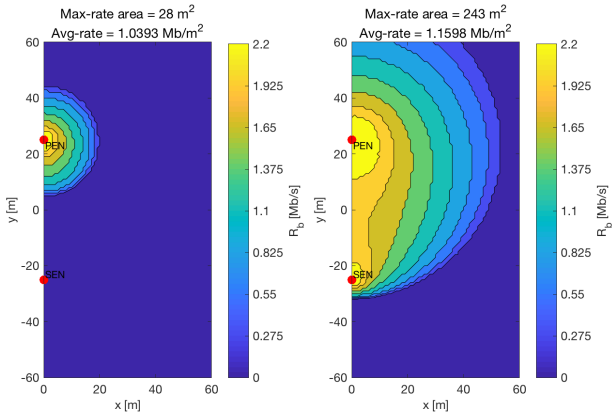

FIGURE 5. AmBC coverage map (passive case; PEN-SEN distance = 50 m) for EIRP = 26 dBm (left-side plot) and EIRP = 33 dBm (right-side plot).

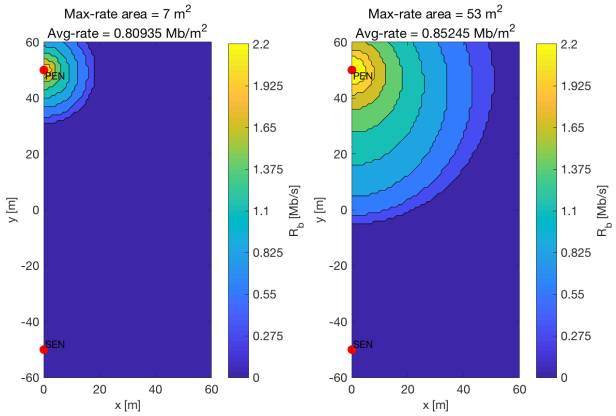

FIGURE 6. AmBC coverage map (passive case; PEN-SEN distance = 100 m) for EIRP = 26 dBm (left-side plot) and EIRP = 33 dBm (right-side plot).

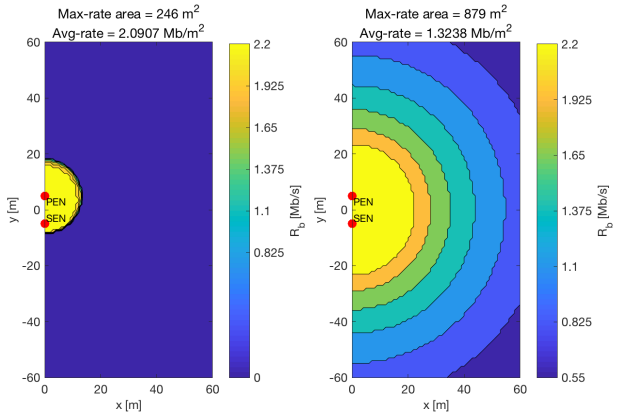

FIGURE 7. AmBC coverage map (passive case; PEN-SEN distance = 10 m) for $\mathcal{P}_{\text{tot}} = -26$ dBm (left-side plot) and $\mathcal{P}_{\text{tot}} = -46$ dBm (right-side plot).

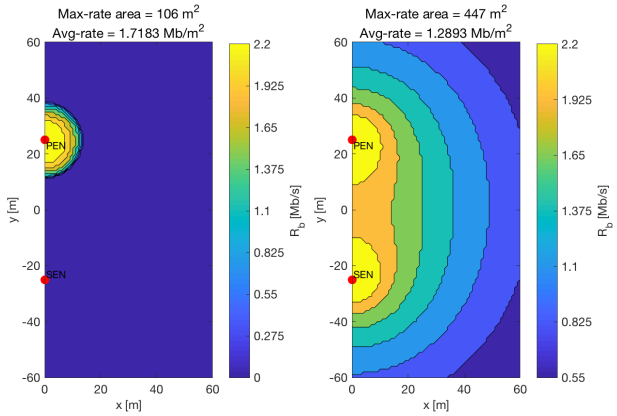

FIGURE 8. AmBC coverage map (passive case; PEN-SEN distance = 50 m) for $\mathcal{P}_{\text{tot}} = -26$ dBm (left-side plot) and $\mathcal{P}_{\text{tot}} = -46$ dBm (right-side plot).

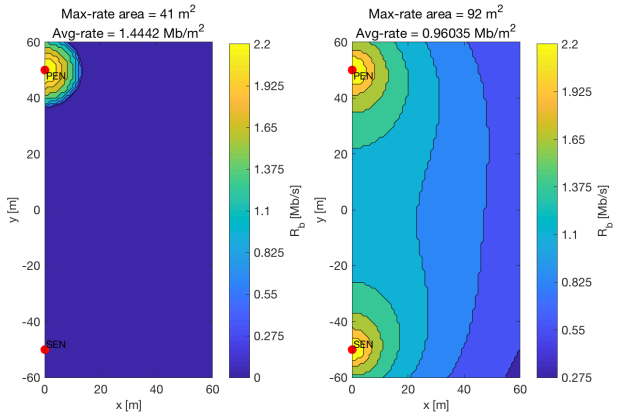

FIGURE 9. AmBC coverage map (passive case; PEN-SEN distance = 100 m) for $\mathcal{P}_{\text{tot}} = -26$ dBm (left-side plot) and $\mathcal{P}_{\text{tot}} = -46$ dBm (right-side plot).

with $0 \leq x \leq 60$ and $-60 \leq y \leq 60$ (in meters). We considered three values of the distance d_{13} between the PEN and SEN, i.e., $d_{13} = 10$ m (short-distance), $d_{13} = 50$ m (medium-distance) and $d_{13} = 100$ m (long-distance), and evaluated the coverage for different values of the primary EIRP $\mathcal{P}_{\text{s}}$ and the power $\mathcal{P}_{\text{tot}}$ consumed by the backscatter sensor. Different colors of the plots correspond to different values of data rate that can be achieved by the sensor, ranging from yellow (Max-rate area) where the sensor achieves the maximum data-rate corresponding to 256-QAM, to deep blue, which represents the area where the backscatter sensor is not able to transmit, due to insufficient energy harvesting. We also evaluated the average transmission rate (Avg-rate) over the whole coverage area.

We first assessed the effect of the primary EIRP: in particular, comparing left and right plots of Figs. 4–6, we note

TABLE 1. Maximum-rate area and average rate of a semi-passive AmBC.

		$d_{13} = 10$ m		$d_{13} = 50$ m		$d_{13} = 100$ m	
		Max-rate area [m^2]	Avg-rate [Mbps/m^2]	Max-rate area [m^2]	Avg-rate [Mbps/m^2]	Max-rate area [m^2]	Avg-rate [Mbps/m^2]
EIRP [dBm]	26	270	1.8155	31	1.2125	8	0.8888
	33	871	1.3707	319	1.2973	55	0.9526
	36	1362	1.4471	1096	1.4490	124	1.1436
$\mathcal{P}_{\text{tot}}$ [dBm]	-26	263	2.1919	131	1.9666	54	1.6702
	-36	871	1.3707	319	1.2973	55	0.9526
	-46	892	1.3360	472	1.3032	109	1.0984
$D_{\min}$	0.75	889	1.4137	343	1.3360	55	0.9910
	0.80	871	1.3707	319	1.2973	55	0.9526
	0.85	844	1.3257	299	1.2565	55	0.9163

TABLE 2. ASEP, channel MSE, and QAM cardinality of a passive AmBC.

EIRP	y	$d_{13} = 10$ m			$d_{13} = 50$ m			$d_{13} = 100$ m		
[dBm]	[m]	ASEP	Δ_{mse}	Q_{d}	ASEP	Δ_{mse}	Q_{d}	ASEP	Δ_{mse}	Q_{d}
26	10	2.24e-4	1.38e-14	128	8.11e-4	1.37e-14	8	inactive	inactive	inactive
26	0	2.21e-4	1.38e-14	256	inactive	inactive	inactive	inactive	inactive	inactive
26	-10	0.89e-4	1.37e-14	32	inactive	inactive	inactive	inactive	inactive	inactive
33	10	0.46e-5	2.75e-15	256	1.97e-4	2.75e-15	128	5.40e-4	2.74e-15	8
33	0	4.85e-7	2.75e-15	256	6.16e-5	2.73e-15	64	2.50e-4	2.74e-15	4
33	-10	0.40e-5	2.73e-15	256	1.42e-4	2.74e-15	64	inactive	inactive	inactive

TABLE 3. ASEP, channel MSE, and QAM cardinality of a semipassive AmBC.

EIRP	y	$d_{13} = 10$ m			$d_{13} = 50$ m			$d_{13} = 100$ m		
[dBm]	[m]	ASEP	Δ_{mse}	Q_{d}	ASEP	Δ_{mse}	Q_{d}	ASEP	Δ_{mse}	Q_{d}
26	10	8.08e-5	1.37e-14	128	3.32e-4	1.37e-14	16	inactive	inactive	inactive
26	0	4.87e-4	1.37e-14	256	inactive	inactive	inactive	inactive	inactive	inactive
26	-10	7.10e-5	1.37e-14	64	inactive	inactive	inactive	inactive	inactive	inactive
33	10	4.96e-4	2.75e-15	256	1.24e-4	2.74e-15	128	5.20e-4	2.74e-15	16
33	0	4.87e-4	2.75e-15	256	1.90e-4	2.74e-15	128	6.56e-4	2.74e-15	8
33	-10	4.77e-4	2.73e-15	256	2.90e-4	2.74e-15	128	inactive	inactive	inactive

that, as expected, increasing values of EIRP allow one to cover a wider area; specifically, from Fig. 5 it is apparent that, when the EIRP increases from 26 to 33 dBm, the Max-rate area increases from 28 to 243 m^2. Moreover, note that the coverage area tends to be more concentrated in proximity of the PEN rather than the SEN, which shows that the prevalent performance limitation of AmBC is, as expected, insufficient illumination from the primary system. Indeed, spatial coverage can be improved by increasing the values of EIRP, as particularly shown by comparing left- and right-side plots of Fig. 5. However, if the distance between the PEN and SEN is further increased, results of Fig. 6 show that the considered values of EIRP are not sufficient to guarantee a uniform coverage to the proposed AmBC system.

In Figs. 7–9, we investigated the effects on the system performance due to different sensor consumption, which is measured by the parameter $\mathcal{P}_{\text{tot}}$, which is varied from -26 down to -46 dBm. It is interesting to note that decreasing $\mathcal{P}_{\text{tot}}$ allows one both to significantly extend the coverage area and also to guarantee a more uniform coverage: in particular, in this case, the backscatter sensor can communicate with high data-rates not only when it is in proximity to the PEN, but also when is closer to the SEN.

With reference to the semi-passive case, for the sake of simplicity, we reported the main results in Tab. 1, where we also investigated the effects of the parameter $D_{\min}$, which limits the duration of the sleep phase in the semi-passive case; in particular, we note that increasing values of $D_{\min}$ correspond to decreasing values of the sleep phase. A careful comparison between Figs. 4–9 and the results reported in Tab. 1 shows that, for given values of EIRP and $\mathcal{P}_{\text{tot}}$, the availability of an energy storage on board allows one to slightly extend the coverage area with respect to the passive case. Basically, there is no significant advantage of using a semi-passive backscatter sensor when the total DC power consumption of the sensor is very low. As regards the sensitivity to $D_{\min}$, it is confirmed that allowing the backscatter sensor to harvests energy for a longer time permits to slightly improve its transmission performance.

In order to corroborate the performance analysis developed in Section III, we reported in Tab. 2 and Tab. 3 the ASEP, the channel estimation MSE Δ_{mse}, and the QAM cardinality, for a passive or semi-passive backscatter sensor, for different

values of EIRP. We considered again three values of the distance between the PEN and SEN, i.e., $d_{13} \in \{10, 50, 100\}$ m, whereas the backscatter sensor is located at coordinates (x, y), with $x = 10$ m and $y \in \{10, 0, -10\}$ m, to take into account the following cases: i) the backscatter sensor is closer to the PEN; ii) the backscatter sensor is equally distant from the PEN and SEN; iii) the backscatter sensor is closer to the SEN. It is apparent that the performance of the ML channel estimator (31) is well below the target value $\Delta_{\text{target}} = 10^{-4}$, for both passive and semipassive backscatter sensor, whereas the ASEP is only slightly greater than $\overline{P}_{1,\text{target}}(e) = 10^{-4}$ in some cases. This result confirms that the suboptimal approach of separating the effects of channel estimation and detection errors allows one to obtain satisfactory results with a reasonable computational effort. As expected, performances are consistently better for the semi-passive case compared to the passive one, especially in terms of ASEP and QAM modulation cardinality.

VI. CONCLUSIONS

This paper dealt with performance analysis and practical designs of both passive and semi-passive secondary backscatter sensors in a C-RAN architecture, which allows one to effectively perform channel estimation and mitigate the DLI generated by the primary system. Capitalizing on detailed signal models of both the harvesting and backscatter processes, we studied the performance of the backscatter system, by taking into account imperfect DLI cancellation, channel estimation, and practical modulation effects. In both the passive and semi-passive cases, the achievable rate of the backscatter transmission was maximized, subject to channel estimation MSE and symbol error rate constraints, by also considering power and energy storage requirements of the sensor. Numerical results showed that a suitable placement of the PEN and SEN is a crucial deployment issue to achieve a large network coverage, while ensuring high data rates through backscattering.

APPENDIX A
PROOF OF THEOREM 1

According to (27), it results that

$$\begin{aligned}\Delta_{\text{mse}} &= \sigma_{d_3}^2 \,\text{tr}\left[(\mathbf{T}\,\mathbf{W}_{\text{DFT}}\,\mathbf{P})^{\dagger}(\mathbf{P}^{\text{T}}\,\mathbf{W}_{\text{IDFT}}\,\mathbf{T}^{\text{H}})^{\dagger}\right] \\ &= \sigma_{d_3}^2 \,\text{tr}[(\mathbf{P}^{\text{T}}\,\mathbf{W}_{\text{IDFT}}\,\mathbf{T}^{\text{H}}\,\mathbf{T}\,\mathbf{W}_{\text{DFT}}\,\mathbf{P})^{-1}] \\ &= \sigma_{d_3}^2 \sum_{j=1}^{L} \lambda_j^{-1}(\mathbf{P}^{\text{T}}\,\mathbf{W}_{\text{IDFT}}\,\mathbf{T}^{\text{H}}\,\mathbf{T}\,\mathbf{W}_{\text{DFT}}\,\mathbf{P}) \end{aligned} \quad (58)$$

where $\sigma_{d_3}^2$ has been defined in the theorem statement and we have observed that

$$(\mathbf{T}\,\mathbf{W}_{\text{DFT}}\,\mathbf{P})^{\dagger} = (\mathbf{P}^{\text{T}}\,\mathbf{W}_{\text{IDFT}}\,\mathbf{T}^{\text{H}}\,\mathbf{T}\,\mathbf{W}_{\text{DFT}}\,\mathbf{P})^{-1}\mathbf{P}^{\text{T}}\,\mathbf{W}_{\text{IDFT}}\,\mathbf{T}^{\text{H}} \quad (59)$$

and, throughout this paper, $\lambda_j(\mathbf{A})$ denotes the jth eigenvalue of an Hermitian matrix $\mathbf{A} \in \mathbb{C}^{J\times J}$, with $\lambda_1(\mathbf{A}) \le \lambda_2(\mathbf{A}) \le \cdots \le \lambda_J(\mathbf{A})$. By using the generalization of the Ostrowski theorem to rectangular matrices [67] and, additionally, observing that $\mathbf{P}^{\text{T}}\,\mathbf{W}_{\text{IDFT}}\,\mathbf{W}_{\text{DFT}}\,\mathbf{P} = \mathbf{I}_L$, one has

$$\begin{aligned}&\lambda_j(\mathbf{P}^{\text{T}}\,\mathbf{W}_{\text{IDFT}}\,\mathbf{T}^{\text{H}}\,\mathbf{T}\,\mathbf{W}_{\text{DFT}}\,\mathbf{P}) = \mu_j, \\ &\qquad \text{with } \lambda_j(\mathbf{T}^{\text{H}}\,\mathbf{T}) \le \mu_j \le \lambda_{j+M-L}(\mathbf{T}^{\text{H}}\,\mathbf{T})\end{aligned} \quad (60)$$

for $j \in \{1, 2, \ldots, L\}$. At this point, we also note that $\mathbf{T}^{\text{H}}\,\mathbf{T}$ is a scaled identity matrix given by

$$\mathbf{T}^{\text{H}}\,\mathbf{T} = M \sum_{n=0}^{B_{\text{t}}-1} \mathbf{T}^{*}(n)\,\mathbf{T}(n) \quad (61)$$

where $\mathbf{T}^{*}(n)\,\mathbf{T}(n) = 2\,\alpha^2\,\mathcal{P}_{\text{s}}\,|b(n)|^2\,\mathbf{I}_M$. Eq. (32) readily comes from (58) and (60), by additionally remembering that all the eigenvalues of the identity matrix are equal to one.

APPENDIX B
PROOF OF THEOREM 2

By virtue of the well-known conditional expectation rule, one obtains

$$\overline{P}(e) = \mathbb{E}_{\widetilde{\mathbf{c}}_{21},\mathbf{s}(n)}\left\{\mathbb{E}_{\widetilde{\mathbf{c}}_{12}}[P(e;n)\,|\,\widetilde{\mathbf{c}}_{21},\mathbf{s}(n)]\right\} \quad (62)$$

where we remember that $\mathbf{h}(n)$ and $\mathbf{K}_{\mathbf{d}_3\mathbf{d}_3}(n)$ have been defined in (17) and (36), respectively. We note that, since $c_{ik}(\ell)$ is a circularly symmetric complex Gaussian random variable by assumption, then $c_{ik}(\ell)$ and $c_{ik}(\ell)\,e^{-j\frac{2\pi}{M}(\ell+\theta_{ik})m}$ have the same probability distribution [68], i.e., $c_{ik}(\ell)\,e^{-j\frac{2\pi}{M}(\ell+\theta_{ik})m} \sim \mathcal{CN}[0, \sigma_{ik}^2/(L_{ik}+1)]$, for any ℓ and m. Thus, one has $C_{ik}(m) \sim \mathcal{CN}(0, \sigma_{ik}^2)$. It is seen from (19) that, even if the time-domain channel taps $\{c_{ik}(\ell)\}_{\ell=0}^{L_{ik}}$ are assumed to be independent, the corresponding DFT samples $C_{ik}(m_1)$ and $C_{ik}(m_2)$ turn out to be correlated, for $m_1 \neq m_2 \in \mathcal{M}$, i.e.,

$$\begin{aligned}\mathbb{E}[C_{ik}(m_1)\,C_{ik}^{*}(m_2)] &= \frac{\sigma_{ik}^2}{L_{ik}+1}\,e^{-j\frac{2\pi}{M}\theta_{ik}(m_1-m_2)} \\ &\quad \cdot \mathsf{D}_{L_{ik}+1}\left(\frac{m_1-m_2}{M}\right)\end{aligned} \quad (63)$$

where, for $x \in \mathbb{R}$, we have defined the Dirichlet function

$$\mathsf{D}_{L_{ik}+1}(x) \triangleq \frac{\sin[\pi(L_{ik}+1)x]}{\sin(\pi x)}\,e^{-j\pi L_{ik}x}. \quad (64)$$

However, it can be verified that $\left|\mathbb{E}[C_{ik}(m_1)\,C_{ik}^{*}(m_2)]\right| \ll \sigma_{ik}^2$ for $m_1 \neq m_2$. Therefore, for the sake of analysis, we will neglect the correlation among the entries of $\widetilde{\mathbf{c}}_{ik}$, by assuming that $\widetilde{\mathbf{c}}_{ik} \sim \mathcal{CN}(\mathbf{0}_M, \sigma_{ik}^2\,\mathbf{I}_M)$. Starting from (39) and resorting to the Chernoff bound [52], one gets (see, also, [69])

$$\begin{aligned}&\mathbb{E}_{\widetilde{\mathbf{c}}_{12}}[P(e;n)\,|\,\widetilde{\mathbf{c}}_{23},\mathbf{s}(n)] \\ &\quad \le A_1\,\mathbb{E}_{\widetilde{\mathbf{c}}_{12}}\left\{\exp\left[-\frac{A_2}{2}\,\alpha^2\,\mathbf{h}^{\text{H}}(n)\,\mathbf{K}_{\mathbf{d}_3\mathbf{d}_3}^{-1}(n)\,\mathbf{h}(n)\right]\right\} \\ &\quad = A_1\,\mathbb{E}_{\widetilde{\mathbf{c}}_{12}}\left\{\exp\left[\widetilde{\mathbf{c}}_{12}^{\text{H}}\,\mathbf{R}(n)\,\widetilde{\mathbf{c}}_{12}\right]\right\} \\ &\quad = \frac{A_1}{\det\left[\mathbf{I}_M + \sigma_{12}^2\,\mathbf{R}(n)\right]}\end{aligned} \quad (65)$$

where

$$\mathbf{R}(n) \triangleq \frac{A_2\,\alpha^2}{2\,M}\,\mathbf{C}_{23}^{*}\,\mathbf{S}^{*}(n)\,\mathbf{K}_{\mathbf{d}_3\mathbf{d}_3}^{-1}(n)\,\mathbf{S}(n)\,\mathbf{C}_{23} \in \mathbb{C}^{M\times M}. \quad (66)$$

and we have used the fact that $|C_{12}(m)|^2$ is exponentially distributed with mean σ_{12}^2. By applying the matrix inversion lemma (see, e.g., [60]) on (36) and exploiting the constant-modulus property of the symbols transmitted by the PEN, one has

$$\begin{aligned}\mathbf{S}^{*}(n)\mathbf{K}_{\mathbf{d}_3\mathbf{d}_3}^{-1}(n)\mathbf{S}(n) &= (2\mathcal{P}_{\mathrm{s}}M)\mathbf{I}_M \\ &\quad -(\mathcal{P}_{\mathrm{s}}M)\mathbf{W}_{\mathrm{DFT}}\mathbf{P}\mathbf{P}^{\mathrm{T}}\mathbf{W}_{\mathrm{IDFT}} \\ &= (2\mathcal{P}_{\mathrm{s}}M)\mathbf{U}\boldsymbol{\Lambda}\mathbf{U}^{\mathrm{H}} \quad (67)\end{aligned}$$

where $\mathbf{U} \in \mathbb{C}^{M\times M}$ is unitary and $\boldsymbol{\Lambda}$ is a block diagonal matrix given by $\boldsymbol{\Lambda} \triangleq \mathrm{diag}(\mathbf{I}_L/2, \mathbf{I}_{M-L})$. Consequently, inequality (65) boils down to

$$\begin{aligned}&\mathbb{E}_{\widetilde{\mathbf{c}}_{12}}[P(e;n)\,|\,\widetilde{\mathbf{c}}_{23}, \mathbf{s}(n)] \\ &\quad \le A_1 \prod_{m=0}^{M-1} \frac{1}{1+A_2\,\alpha^2\,\mathcal{P}_{\mathrm{s}}\,\sigma_{12}^2\,\lambda_m(\boldsymbol{\Lambda}^{1/2}\,\mathbf{U}^{\mathrm{H}}\,\mathbf{C}_{23}\,\mathbf{C}_{23}^{*}\mathbf{U}\,\boldsymbol{\Lambda}^{1/2})} \quad (68)\end{aligned}$$

where we have also used the facts that

$$\begin{aligned}&\det\left(\mathbf{I}_M + A_2\alpha^2\mathcal{P}_{\mathrm{s}}\sigma_{12}^2\mathbf{C}_{23}^{*}\mathbf{U}\boldsymbol{\Lambda}\mathbf{U}^{\mathrm{H}}\mathbf{C}_{23}\right) \\ &\quad = \det\left(\mathbf{I}_M + A_2\alpha^2\mathcal{P}_{\mathrm{s}}\sigma_{12}^2\boldsymbol{\Lambda}^{1/2}\mathbf{U}^{\mathrm{H}}\mathbf{C}_{23}\mathbf{C}_{23}^{*}\mathbf{U}\boldsymbol{\Lambda}^{1/2}\right). \quad (69)\end{aligned}$$

and the determinant of a matrix is equal to the product of its eigenvalues. By applying the Ostrowski theorem [59], it results that

$$|C_{23}(m)|^2/2 \le \lambda_m(\boldsymbol{\Lambda}^{1/2}\,\mathbf{U}^{\mathrm{H}}\,\mathbf{C}_{23}\,\mathbf{C}_{23}^{*}\mathbf{U}\,\boldsymbol{\Lambda}^{1/2}) \le |C_{23}(m)|^2 \quad (70)$$

and, therefore, we get the upper bound

$$\begin{aligned}&\mathbb{E}_{\widetilde{\mathbf{c}}_{12}}[P(e;n)\,|\,\widetilde{\mathbf{c}}_{23}, \mathbf{s}(n)] \\ &\quad \le A_1 \prod_{m=0}^{M-1} \frac{1}{1+\frac{A_2}{2}\,\alpha^2\,\mathcal{P}_{\mathrm{s}}\,\sigma_{12}^2\,|C_{23}(m)|^2}. \quad (71)\end{aligned}$$

From (62) and (71), one obtains the inequality

$$\overline{P}(e) \le A_1 \prod_{m=0}^{M-1} \mathbb{E}_{C_{23}(m)}\left[\frac{1}{1+\frac{A_2}{2}\,\alpha^2\,\mathcal{P}_{\mathrm{s}}\,\sigma_{12}^2\,|C_{23}(m)|^2}\right]. \quad (72)$$

Since the random variable $|C_{23}(m)|^2$ is exponentially distributed with mean σ_{23}^2, one has

$$\begin{aligned}&\mathbb{E}_{C_{23}(m)}\left[\frac{1}{1+\frac{A_2}{2}\alpha^2\mathcal{P}_{\mathrm{s}}\sigma_{12}^2|C_{23}(m)|^2}\right] \\ &\quad = -\frac{\exp\left(\frac{1}{\frac{A_2}{2}\alpha^2\mathcal{P}_{\mathrm{s}}\sigma_{12}^2\sigma_{23}^2}\right)}{\frac{A_2}{2}\alpha^2\mathcal{P}_{\mathrm{s}}\sigma_{12}^2\sigma_{23}^2} \\ &\qquad \cdot\mathrm{Ei}\left(-\frac{1}{\frac{A_2}{2}\alpha^2\mathcal{P}_{\mathrm{s}}\sigma_{12}^2\sigma_{23}^2}\right) \quad (73)\end{aligned}$$

where $\mathrm{Ei}(x)$ is defined in (42). The upper bound (40) follows after simple manipulations by substituting (73) in (72).

APPENDIX C
PROOF OF THEOREM 3

The optimization problem (52) can be solved in three stages. In the first one, the objective function in (52) is maximized with respect to (w.r.t.) Q_{d}, for fixed values of α, T_{o}, T_{t}, and T_{d}, thus boiling down to

$$\begin{aligned}&\arg\max_{Q_{\mathrm{d}}} \ \frac{T_{\mathrm{d}}\,\log_2(Q_{\mathrm{d}})}{T_{\mathrm{f}}} \ \text{s.t.} \\ &\qquad \overline{P}_{\mathrm{upper}}(e) \le \overline{P}_{\mathrm{target}}(e) \ \text{ and } \ Q_{\mathrm{d}} \le Q_{\max}. \quad (74)\end{aligned}$$

For the sake of simplicity, we neglect the dependence of A_1 on Q_{d} in (40), i.e., we assume that $A_1 \approx 4$. So doing, the *soft* solution of (74) is given by

$$Q_{\mathrm{d}}^{\star}(\alpha) = \min\left(1+\frac{\alpha^2}{\Gamma_{\mathrm{d}}}, Q_{\max}\right) \quad (75)$$

with $\Gamma_{\mathrm{d}} \triangleq \left\{\sigma_{v_3}^2 f^{-1}\left([\overline{P}_{\mathrm{target}}(e)/4]^{1/M}\right)\right\}/(3\,\mathcal{P}_{\mathrm{s}}\,\sigma_{12}^2\,\sigma_{23}^4)$.

If the training symbols transmitted by the backscatter sensor are PSK, the channel MSE is given by (34) and $\Delta_{\mathrm{mse}} \le \Delta_{\mathrm{target}}$ is tantamount to $T_{\mathrm{t}} \ge \Gamma_{\mathrm{t}}/\alpha^2$, with $\Gamma_{\mathrm{t}} \triangleq (\sigma_{d_3}^2\,L\,T_{\mathrm{s}})/(M\,\mathcal{P}_{\mathrm{s}}\,\Delta_{\mathrm{target}})$. Hence, for a given value of α, the optimal value of T_{t} turns out to be

$$T_{\mathrm{t}}^{\star}(\alpha) = \frac{\Gamma_{\mathrm{t}}}{\alpha^2} \quad (76)$$

provided that $\Gamma_{\mathrm{t}}/\alpha^2 \le T_{\mathrm{f}}$, and $T_{\mathrm{d}}^{\star}(\alpha) = T_{\mathrm{f}} - T_{\mathrm{t}}^{\star}(\alpha)$ is the corresponding optimal value of T_{d}.

In the second stage, we plug (75) and (76) into problem (52) and consider the maximization of the corresponding cost function w.r.t. α and T_{o}, hence obtaining, after simple algebraic manipulations, the simplified problem

$$\begin{aligned}&\arg\max_{\alpha,T_{\mathrm{o}}} \ \left(1-\frac{\Gamma_{\mathrm{t}}}{\alpha^2\,T_{\mathrm{f}}}\right)\log_2\left[Q_{\mathrm{d}}^{\star}(\alpha)\right] \\ &\text{s.t.} \ \frac{T_{\mathrm{o}}}{T_{\mathrm{f}}} \le I_{\max}, \quad \alpha^2 \le \alpha_{\max}^2 + \frac{T_{\mathrm{o}}}{T_{\mathrm{f}}}, \quad \alpha^2 \ge \alpha_{\mathrm{storage}}^2 + \frac{T_{\mathrm{o}}}{T_{\mathrm{f}}} \\ &\qquad \frac{\Gamma_{\mathrm{t}}}{\alpha^2} \le T_{\mathrm{f}}, \quad 0<\alpha\le 1, \ \text{and} \ T_{\mathrm{o}} > 0 \quad (77)\end{aligned}$$

with $I_{\max} \triangleq (1-D_{\min})/D_{\min}$. For a given value of α, the constraints of problem (77) form a non-empty feasible set (i.e., all the constraints involving T_{o} are fulfilled) if $\alpha_{\max}^2 \ge \alpha_{\mathrm{storage}}^2$ and $\alpha_{\max}^2 < \alpha^2 \le \alpha_{\max}^2 + I_{\max}$: in this case, the optimal value of T_{o} is given by

$$T_{\mathrm{o}}^{\star}(\alpha) = (\alpha^2 - \alpha_{\max}^2)T_{\mathrm{f}}. \quad (78)$$

In the last stage, we substitute (78) in (77), thus obtaining the optimal value of α as the solution of the problem

$$\arg\max_{\alpha}\left(1-\frac{\Gamma_{\rm t}}{\alpha^2 T_{\rm f}}\right)\log_2\left[Q_{\rm d}^{\star}(\alpha)\right]$$
$$\text{s.t.}\,\frac{\Gamma_{\rm t}}{\alpha^2}\leq T_{\rm f},\quad \alpha_{\max}^2<\alpha^2\leq\alpha_{\max}^2+I_{\max},\ \text{and}\ 0<\alpha\leq 1. \tag{79}$$

It can be verified that problem (79) admits the solution

$$\alpha^{\star}=\min\left[\sqrt{\alpha_{\max}^2+I_{\max}},\sqrt{\Gamma_{\rm d}(Q_{\max}-1)},1\right] \tag{80}$$

provided that $\Gamma_{\rm t}/T_{\rm f}\leq\alpha_{\max}^2+I_{\max}$, It results that $Q_{\rm d}^{\star}=Q_{\rm d}^{\star}(\alpha^{\star})$, $T_{\rm o}^{\star}=T_{\rm o}^{\star}(\alpha^{\star})$, $T_{\rm t}^{\star}=T_{\rm t}^{\star}(\alpha^{\star})$, and $T_{\rm d}^{\star}=T_{\rm d}^{\star}(\alpha^{\star})$.

REFERENCES

[1] *Overview of the Internet of Things (IoT)*, document ITU-T Rec. Y.2060 (06/2012), Jun. 2012.

[2] M. McHenry, E. Livsics, T. Nguyen, and N. Majumdar, "XG dynamic spectrum access field test results [topics in radio communications]," *IEEE Commun. Mag.*, vol. 45, no. 6, pp. 51–57, Jun. 2007.

[3] S. Haykin, "Cognitive radio: Brain-empowered wireless communications," *IEEE J. Sel. Areas Commun.*, vol. 23, no. 2, pp. 201–220, Feb. 2005.

[4] A. Goldsmith, E. Biglieri, and L. J. Greenstein, *Principles of Cognitive Radio*. New York, NY, USA: Cambridge Univ. Press, 2013.

[5] P. Kamalinejad, C. Mahapatra, Z. Sheng, S. Mirabbasi, V. C. M. Leung, and Y. L. Guan, "Wireless energy harvesting for the Internet of Things," *IEEE Commun. Mag.*, vol. 53, no. 6, pp. 102–108, Jun. 2015.

[6] M. Erol-Kantarci and H. T. Mouftah, "Suresense: Sustainable wireless rechargeable sensor networks for the smart grid," *IEEE Wireless Commun.*, vol. 19, no. 3, pp. 30–36, Jun. 2012.

[7] M. Erol-Kantarci and H. T. Mouftah, "Mission-aware placement of RF-based power transmitters in wireless sensor networks," in *Proc. ISCC*, Cappadocia, Turkey, Jul. 2012, pp. 12–17.

[8] M. Erol-Kantarci and H. T. Mouftah, "DRIFT: Differentiated RF power transmission for wireless sensor network deployment in the smart grid," in *Proc. Globecom Workshops*, Dec. 2012, pp. 1491–1495.

[9] G. Yang, C. K. Ho, and Y. L. Guan, "Multi-antenna wireless energy transfer for backscatter communication systems," *IEEE J. Sel. Areas Commun.*, vol. 33, no. 12, pp. 2974–2987, Dec. 2015.

[10] K. Han and K. Huang, "Wirelessly powered backscatter communication networks: Modeling, coverage, and capacity," *IEEE Trans. Wireless Commun.*, vol. 16, no. 4, pp. 2548–2561, Apr. 2017.

[11] J. Kimionis, A. Bletsas, and J. N. Sahalos, "Increased range bistatic scatter radio," *IEEE Trans. Commun.*, vol. 62, no. 3, pp. 1091–1104, Mar. 2014.

[12] E. Kampianakis, J. Kimionis, K. Tountas, C. Konstantopoulos, E. Koutroulis, and A. Bletsas, "Wireless environmental sensor networking with analog scatter radio and timer principles," *IEEE Sensors J.*, vol. 14, no. 10, pp. 3365–3376, Oct. 2014.

[13] N. Fasarakis-Hilliard, P. N. Alevizos, and A. Bletsas, "Coherent detection and channel coding for bistatic scatter radio sensor networking," *IEEE Trans. Commun.*, vol. 63, no. 5, pp. 1798–1810, May 2015.

[14] P. N. Alevizos, A. Bletsas, and G. N. Karystinos, "Noncoherent short packet detection and decoding for scatter radio sensor networking," *IEEE Trans. Commun.*, vol. 65, no. 5, pp. 2128–2140, May 2017.

[15] S. Bi, C. K. Ho, and R. Zhang, "Wireless powered communication: Opportunities and challenges," *IEEE Commun. Mag.*, vol. 53, no. 4, pp. 117–125, Apr. 2015.

[16] X. Lu, P. Wang, D. Niyato, D. I. Kim, and Z. Han, "Wireless networks with RF energy harvesting: A contemporary survey," *IEEE Commun. Surveys Tuts.*, vol. 17, no. 2, pp. 757–789, 2nd Quart., 2015.

[17] S. Lee and R. Zhang, "Cognitive wireless powered network: Spectrum sharing models and throughput maximization," *IEEE Trans. Cogn. Commun. Netw.*, vol. 1, no. 3, pp. 335–346, Sep. 2015.

[18] S. Bi, Y. Zeng, and R. Zhang, "Wireless powered communication networks: An overview," *IEEE Wireless Commun.*, vol. 23, no. 2, pp. 10–18, Apr. 2016.

[19] V. Liu, A. Parks, V. Talla, S. Gollakota, D. Wetherall, and J. R. Smith, "Ambient backscatter: Wireless communication out of thin air," in *Proc. ACM SIGCOMM*, Hong Kong, Aug. 2013, pp. 39–50.

[20] B. Kellogg, A. Parks, S. Gollakota, J. R. Smith, and D. Wetherall, "Wi-Fi backscatter: Internet connectivity for RF-powered devices," in *Proc. ACM SIGCOMM*, Chicago, Illinois, USA, Aug. 2014, pp. 607–618.

[21] D. Bharadia, K. R. Joshi, M. Kotaru, and S. Katti, "Backfi: High throughput WIFI backscatter," in *Proc. ACM SIGCOMM*, London, United Kingdom, Aug. 2015, pp. 283–296.

[22] V. Iyer, V. Talla, B. Kellogg, S. Gollakota, and J. Smith, "Inter-technology backscatter: Towards Internet connectivity for implanted devices," in *Proc. ACM SIGCOMM*, Florianopolis, Brazil, Aug. 2016, pp. 356–369.

[23] P. Zhang, M. Rostami, P. Hu, and D. Ganesan, "Enabling practical backscatter communication for on-body sensors," in *Proc. ACM SIGCOMM*, Florianopolis, Brazil, Aug. 2016, pp. 370–383.

[24] A. Wang, V. Iyer, V. Talla, J. R. Smith, and S. Gollakota, "FM backscatter: Enabling connected cities and smart fabrics," in *Proc. USENIX NSDI*, Boston, MA, USA, Mar. 2017, pp. 243–258.

[25] Z. Ma, T. Zeng, G. Wang, and F. Gao, "Signal detection for ambient backscatter system with multiple receiving antennas," in *Proc. IEEE 14th Can. Workshop Inf. Theory (CWIT)*, St. John's, NL, Canada, Jul. 2015, pp. 50–53.

[26] K. Lu, G. Wang, F. Qu, and Z. Zhong, "Signal detection and BER analysis for RF-powered devices utilizing ambient backscatter," in *Proc. Int. Conf. Wireless Commun. Signal Process. (WCSP)*, Nanjing, China, Oct. 2015, pp. 1–5.

[27] G. Wang, F. Gao, Z. Dou, and C. Tellambura, "Uplink detection and BER analysis for ambient backscatter communication systems," in *Proc. IEEE Global Commun. Conf. (GLOBECOM)*, San Diego, CA, USA, Dec. 2015, pp. 1–6.

[28] G. Wang, F. Gao, R. Fan, and C. Tellambura, "Ambient backscatter communication systems: Detection and performance analysis," *IEEE Trans. Commun.*, vol. 64, no. 11, pp. 4836–4846, Nov. 2016.

[29] J. Qian, F. Gao, G. Wang, S. Jin, and H. Zhu, "Noncoherent detections for ambient backscatter system," *IEEE Trans. Wireless Commun.*, vol. 16, no. 3, pp. 1412–1422, Mar. 2017.

[30] G. Yang and Y.-C. Liang, "Backscatter communications over ambient OFDM signals: Transceiver design and performance analysis," in *Proc. IEEE Global Commun. Conf. (GLOBECOM)*, Washington, DC, USA, Dec. 2016, pp. 1–6.

[31] G. Yang, Y.-C. Liang, R. Zhang, and Y. Pei, "Modulation in the air: Backscatter communication over ambient OFDM carrier," *IEEE Trans. Commun.*, vol. 66, no. 3, pp. 1219–1233, Mar. 2018.

[32] D. Darsena, G. Gelli, and F. Verde, "Modeling and performance analysis of wireless networks with ambient backscatter devices," *IEEE Trans. Commun.*, vol. 65, no. 4, pp. 1797–1814, Apr. 2017.

[33] D. T. Hoang, D. Niyato, P. Wang, D. I. Kim, and Z. Han, "Ambient backscatter: A new approach to improve network performance for RF-powered cognitive radio networks," *IEEE Trans. Commun.*, vol. 65, no. 9, pp. 3659–3674, Sep. 2017.

[34] H. Guo, Q. Zhang, S. Xiao, and Y.-C. Liang, "Exploiting multiple antennas for cognitive ambient backscatter communication," *IEEE Internet Things J.*, vol. 6, no. 1, pp. 765–775, Feb. 2019.

[35] C. Boyer and S. Roy, "Backscatter communication and RFID: Coding, energy, and MIMO analysis," *IEEE Trans. Commun.*, vol. 62, no. 3, pp. 770–785, Mar. 2014.

[36] Y. D. Beyene, *et. al.*, "NB-IoT technology overview and experience from cloud-RAN implementation," *IEEE Wireless Commun.*, vol. 24, no. 3, pp. 26–32, Jun. 2017.

[37] A. Checko *et al.*, "Cloud RAN for mobile networks—A technology overview," *IEEE Commun. Surveys Tuts.*, vol. 17, no. 1, pp. 405–426, 1st Quart., 2014.

[38] T. Q. Quek, M. Peng, O. Simeone, and W. Yu, *Cloud Radio Access Networks: Principles, Technologies, and Applications*. Cambridge, U.K.: Cambridge Univ. Press, 2017.

[39] N. Van Huynh, D. T. Hoang, D. Niyato, P. Wang, and D. I. Kim, "Optimal time scheduling for wireless-powered backscatter communication networks," *IEEE Wireless Commun. Lett.*, vol. 7, no. 5, pp. 820–823, Oct. 2018.

[40] S. Ma, G. Wang, R. Fan, and C. Tellambura, "Blind channel estimation for ambient backscatter communication systems," *IEEE Commun. Lett.*, vol. 22, no. 6, pp. 1296–1299, Jun. 2018.

[41] Q. Zhang, H. Guo, Y.-C. Liang, and X. Yuan, "Constellation learning-based signal detection for ambient backscatter communication systems," *IEEE J. Sel. Areas Commun.*, vol. 37, no. 2, pp. 452–463, Feb. 2019.
[42] C. Zhang, G. Wang, P. D. Diamantoulakis, F. Gao, and G. K. Karagiannidis. (2018). "Interference-free transceiver design and signal detection for ambient backscatter communication systems over frequency-selective channels." [Online]. Available: https://arxiv.org/abs/1812.11278
[43] B. Lyu, C. You, Z. Yang, and G. Gui, "The optimal control policy for RF-powered backscatter communication networks," *IEEE Trans. Veh. Technol.*, vol. 67, no. 3, pp. 2804–2808, Mar. 2018.
[44] O. Bello and S. Zeadally, "Intelligent device-to-device communication in the Internet of Things," *IEEE Syst. J.*, vol. 10, no. 3, pp. 1172–1182, Sep. 2016.
[45] H. Shariatmadari *et al.*, "Machine-type communications: Current status and future perspectives toward 5G systems," *IEEE Commun. Mag.*, vol. 53, no. 9, pp. 10–17, Sep. 2015.
[46] F. Wang and X. Zhang, "Joint WiFi offloading and resource allocation for RF-powered wireless networks assisted by ambient backscatter," in *Proc. Int. Conf. Commun. (ICC)*, Kansas City, MO, USA, May 2018, pp. 1–6.
[47] F. A. Khan, H. He, J. Xue, and T. Ratnarajah, "Performance analysis of cloud radio access networks with distributed multiple antenna remote radio heads," *IEEE Trans. Signal Process.*, vol. 63, no. 18, pp. 4784–4799, Sep. 2015.
[48] M. Mohammadi, H. A. Suraweera, and C. Tellambura, "Uplink/downlink rate analysis and impact of power allocation for full-duplex cloud-RANs," *IEEE Trans. Wireless Commun.*, vol. 17, no. 9, pp. 5774–5788, Sep. 2018.
[49] T. Le, K. Mayaram, and T. Fiez, "Efficient far-field radio frequency energy harvesting for passively powered sensor networks," *IEEE J. Solid-State Circuits*, vol. 43, no. 5, pp. 1287–1302, May 2008.
[50] Z. Wang and G. B. Giannakis, "Wireless multicarrier communications," *IEEE Signal Process. Mag.*, vol. 17, no. 3, pp. 29–48, May 2000.
[51] R. M. Gray, "Toeplitz and circulant matrices: A review," *Found. Trends Commun. Inf. Theory*, vol. 2, no. 3, pp. 155–239, 2006.
[52] J. G. Proakis, *Digital Communications*. New York, NY, USA: McGraw-Hill, 2001.
[53] H. Stockman, "Communication by means of reflected power," *Proc. IRE*, vol. 36, no. 10, pp. 1196–1204, Oct. 1948.
[54] S. J. Thomas, E. Wheeler, J. Teizer, and M. S. Reynolds, "Quadrature amplitude modulated backscatter in passive and semipassive UHF RFID systems," *IEEE Trans. Microw. Theory Techn.*, vol. 60, no. 4, pp. 1175–1182, Apr. 2012.
[55] S. Thomas and M. S. Reynolds, "A 96 Mbit/sec, 15.5 pJ/bit 16-QAM modulator for UHF backscatter communication," in *Proc. IEEE Int. Conf. RFID*, Orlando, FL, USA, Apr. 2012, pp. 185–190.
[56] M. Morelli and U. Mengali, "A comparison of pilot-aided channel estimation methods for OFDM systems," *IEEE Trans. Signal Process.*, vol. 49, no. 12, pp. 3065–3073, Dec. 2001.
[57] B. Smida and S. Khaledian, "ReflectFX: In-band full-duplex wireless communication by means of reflected power," *IEEE Trans. Commun.*, vol. 65, no. 5, pp. 2207–2219, May 2017.
[58] R. C. Hansen, "Relationships between antennas as scatterers and as radiators," *Proc. IEEE*, vol. 77, no. 5, pp. 659–662, May 1989.
[59] R. A. Horn and C. R. Johnson, *Matrix Analysis*. Cambridge, U.K.: Cambridge Univ. Press, 1990.
[60] S. Kay, *Fundamentals of Statistical Signal Processing: Detection Theory*. Englewood Cliffs, NJ, USA: Prentice-Hall, 1993.
[61] X. Tang, M.-S. Alouini, and A. J. Goldsmith, "Effect of channel estimation error on M-QAM BER performance in Rayleigh fading," *IEEE Trans. Commun.*, vol. 47, no. 12, pp. 1856–1864, Dec. 1999.
[62] K. Kurokawa, "Power waves and the scattering matrix," *IEEE Trans. Microw. Theory Techn.*, vol. 13, no. 2, pp. 194–202, Mar. 1965.
[63] *Powercast Wireless Power Calculator (Version 1.5)*. Accessed: May 3, 2019. [Online]. Available: http://www.powercastco.com/power-calculator
[64] T. Rappaport, *Wireless Communications: Principles and Practice*, 2nd ed. Upper Saddle River, NJ, USA: Prentice-Hall, 2001.
[65] J. Fraden, *Handbook of Modern Sensors: Physics, Designs, and Applications*. Cham, Switzerland: Springer, 2016.
[66] U. Karthaus and M. Fischer, "Fully integrated passive UHF RFID transponder IC with 16.7-μW minimum RF input power," *IEEE J. Solid-State Circuits*, vol. 38, no. 10, pp. 1602–1608, Oct. 2003.
[67] N. J. Higham and S. H. Cheng, "Modifying the inertia of matrices arising in optimization," *Linear Algebra Appl.*, vols. 275–276, pp. 261–279, May 1998.
[68] B. Picinbono, "On circularity," *IEEE Trans. Signal Process.*, vol. 42, no. 12, pp. 3473–3482, Dec. 1994.
[69] N. R. Goodman, "Statistical analysis based on a certain multivariate complex Gaussian distribution (an introduction)," *Ann. Math. Statist.*, vol. 34, no. 1, pp. 152–177, 1963.

DONATELLA DARSENA (M'06–SM'16) received the Dr.Eng. degree *(summa cum laude)* in telecommunications engineering and the Ph.D. degree in electronic and telecommunications engineering from the University of Napoli Federico II, Italy, in 2001 and 2005, respectively.

From 2001 to 2002, she was an Engineer with the Telecommunications, Peripherals and Automotive Group, STMicroelectronics, Milan, Italy. Since 2005, she has been an Assistant Professor with the Department of Engineering, Parthenope University, Italy. Her research activities lie in the areas of statistical signal processing, digital communications, and communication systems. Her current research interests include equalization, channel identification, narrowband-interference suppression for multicarrier systems, space–time processing for cooperative communications systems and cognitive communications systems, and software-defined networks. She has been serving as an Associate Editor for the IEEE COMMUNICATIONS LETTERS, since 2016, and IEEE ACCESS, since 2018.

GIACINTO GELLI (M'18) was born in Napoli, Italy, in 1964. He received the Dr.Eng. degree *(summa cum laude)* in electronic engineering and the Ph.D. degree in computer science and electronic engineering from the University of Napoli Federico II, in 1990 and 1994, respectively.

From 1994 to 1998, he was an Assistant Professor with the Department of Information Engineering, Second University of Naples. He also held teaching positions at Parthenope University. Since 1998, he has been an Associate Professor with the Department of Electrical Engineering and Information Technology, University of Napoli Federico II, where he has been a Full Professor of telecommunications, since 2006. His research interests include the broad area of signal and array processing for communications, with current emphasis on multicarrier modulation systems and space–time techniques for cooperative and cognitive communications systems.

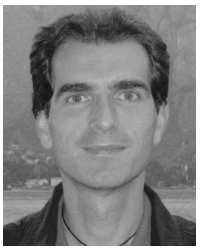

FRANCESCO VERDE (M'10–SM'14) was born in Santa Maria Capua Vetere, Italy, in 1974. He received the Dr.Eng. degree *(summa cum laude)* in electronic engineering from the Second University of Naples, Italy, in 1998, and the Ph.D. degree in information engineering from the University of Napoli Federico II, in 2002.

Since 2002, he has been with the University of Napoli Federico II. He first served as an Assistant Professor of signal theory and mobile communications and since 2011, he has been serving as an Associate Professor of telecommunications with the Department of Electrical Engineering and Information Technology. His research interests include orthogonal/non-orthogonal multiple-access techniques, space–time processing for cooperative/cognitive communications, wireless systems optimization, and software-defined networks. He is also an elected member of the IoT Special Internet Group (SIG) of the IEEE Signal Processing Society for the term 2018–2020. He has been involved in several technical program committees of the major IEEE conferences in signal processing and wireless communications. He was an Associate Editor of the IEEE TRANSACTIONS ON SIGNAL PROCESSING, from 2010 to 2014, and the IEEE SIGNAL PROCESSING LETTERS, from 2014 to 2018, and the Guest Editor of the *EURASIP Journal on Advances in Signal Processing*, in 2010, and *Sensors* (MDPI), in 2018. He has been serving as an Associate Editor for the IEEE TRANSACTIONS ON COMMUNICATIONS, since 2017, and a Senior Area Editor for the IEEE SIGNAL PROCESSING LETTERS, since 2018.